




Review

3D Imaging based on Depth Measurement Technologies

Ni Chen ^{1,†} , Chao Zuo ^{2,†} , Edmund Y. Lam ³ , and Byoungcho Lee ^{1,*}

¹ School of Electrical Engineering, Seoul National University, Gwanak-Gu Gwanakro 1, Seoul 151-744, Korea; chenni@snu.ac.kr(N.C.); byoungcho@snu.ac.kr(B.L.)

² Jiangsu Key Laboratory of Spectral Imaging & Intelligent Sense, Nanjing University of Science and Technology, Nanjing, Jiangsu Province 210094, China; surpasszuo@163.com(C.Z.)

³ Department of Electrical and Electronic Engineering, The University of Hong Kong, Pokfulam, Hong Kong; elam@eee.hku.hk(E.L.)

* Correspondence: byoungcho@snu.ac.kr; Tel.: +82-2-880-7245

† These authors contributed equally to this work.

Abstract: Three-dimensional (3D) imaging has attracted more and more interests because of its widespread applications, especially in information and life science. These techniques can be broadly divided into two types: ray-based and wavefront-based 3D imaging. Issues such as imaging quality and system complexity of these techniques limit the applications significantly, and therefore many investigations have focused on 3D imaging from depth measurements. This paper presents an overview of 3D imaging from depth measurements, and provides a summary of the connection between these the ray-based and wavefront-based 3D imaging techniques.

Keywords: Three-dimensional imaging; computational imaging; light field; holography; phase imaging

1. Introduction

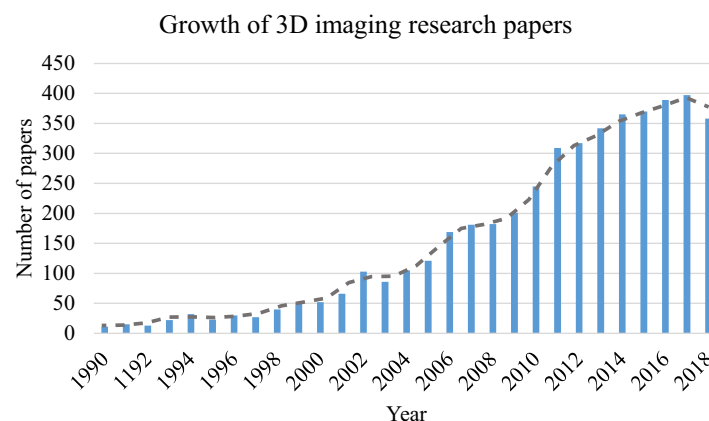


Figure 1. Number of papers with a title containing “3D imaging” in Google Scholar [1] during the past decades.

Beyond the conventional two-dimensional (2D) imaging and photography, 3D imaging, which carries more information of the world, has a wide range of applications, particularly in the fields of life science [2] and information science [3]. Therefore, it has been attracting more and more attention in recent years [4,5]. Figure 1 shows the growth of 3D imaging related research papers during the past decades in Google Scholar [1], showing increasing interest in 3D imaging.

When we refer to 3D information, we usually mean that in addition to the 2D images, the depth or shape of the objects is also captured. The 3D information of an object is contained in the wave’s intensity

and phase of the light wave over it. 3D imaging, in some cases, can be regarded as both amplitude and phase imaging, which is also known as wavefront imaging. The phase of an electromagnetic wave is invisible, but it is inevitably changed as it passes through an object, which induces intensity changes. This can be illustrated in Fig. 2. The shape of the object, including both the depth or surface, bends or distorts the light that goes through it. The amount of light bent behaves as phase delay, and reflects the surface topology [6] or the shape and density [7] of the object. The detected intensity image of the wavefront thus carries the 3D information of the object, resulting in specific intensity patterns. The brighter areas reflect light energy concentration and dimmer areas reflect light energy spreading out, as shown in Fig. 2.

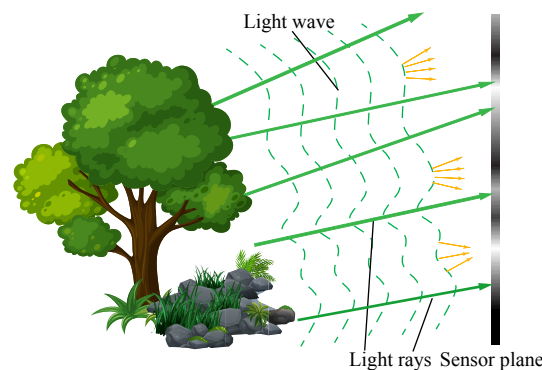


Figure 2. Relationship between light ray and wave.

As is commonly known, light wave and ray are used to describe light in different levels, while Eikonal equation gives a link between ray optics and wave optics [8]. Wave optics is used to describe phenomena where diffraction and interference are important, while ray optics is where light can be considered to be a ray. In many imaging cases, treating light as ray is enough to solve the problems. From the viewpoint of ray optics, as shown in Fig. 2, the directions of the reflected light rays are determined by the normal to the object surface at the incidence point [9]. Therefore, By recording the light rays coming from the objects with their directions, we can also reconstruct its 3D surface shape. Imaging with light rays along with its direction is called light field imaging [10,11]. In this paper, we name it as “light ray field” to distinguish from “light wavefront field”. Based on the above description, 3D imaging can be regarded as light ray and phase (wavefront) imaging to some extent.

The applications of 3D imaging are extremely wide. Figure 3 shows several of them. The wavefront-based 3D imaging is efficient for viewing structures in microscopy [12] and medical applications. The light ray field, which can produce multiple view images with parallax, is a practical and commercialized way for both stereoscopic and auto-stereoscopic 3D displays [13,14]. Benefiting from 3D imaging, hologram synthesis, which sometimes combines the wavefront-based and ray-based light field techniques, can make a hologram of the real world 3D scene under incoherent illumination, making holographic 3D display more realizable [15,16].

However, both “light ray” and “phase” of the wavefront cannot be detected directly. Based on the fact that intensity measurements carry the 3D information about the object wave, and benefiting from computational imaging [17], 3D imaging becomes prosperous in recent decades [17]. Many techniques have been developed in phase imaging, including coherent diffraction imaging [18], phase retrieval [19–21], holography [22,23], time of flight (TOF) [24], and structured-light [25]. For light ray imaging, there are also a lot of techniques such as stereo imaging [26], and light field [10,27] (Stereo imaging can be regarded as an extreme light field imaging). Considering the imaging quality and the system complexity, recently, many investigations have been conducted on 3D imaging from depth measurements. In this paper, we present an overview of ray-based and wavefront-based 3D imaging using depth measurement techniques. For each type, we briefly introduce the theory and its technical development in Section 2. Then we review the state-of-the-art depth measurement based techniques of

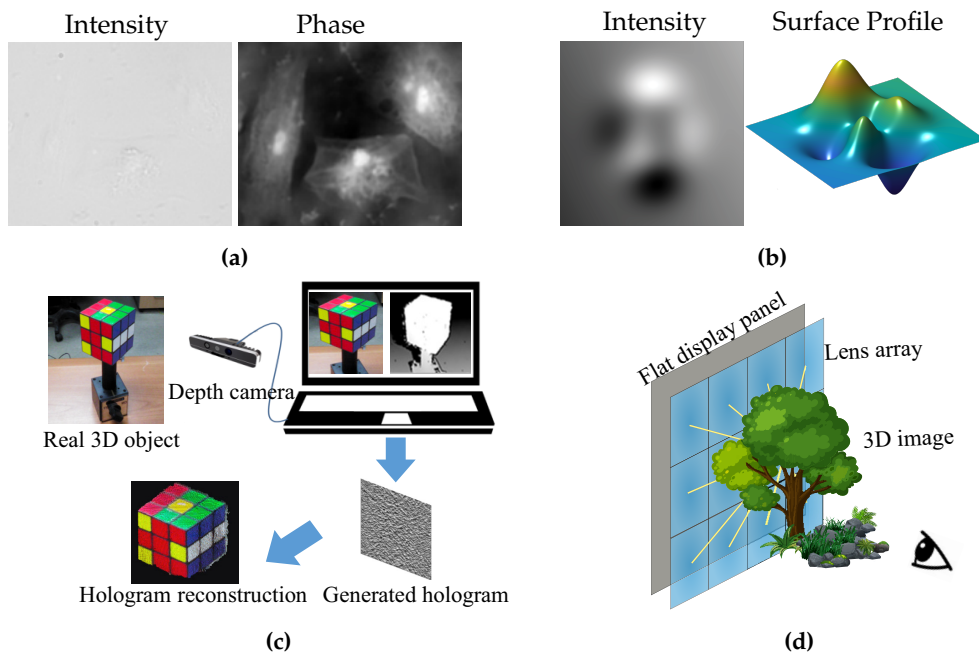


Figure 3. Applications of 3D imaging for (a) microscopy, (b) surface measurement, (c) holographic display, and (d) light field display.

the two types respectively in Sections 3 and 4. Due to the close connection of the ray and wave optics, there is no clear boundary between the two types of 3D imaging techniques. In Section 5, we show comparisons between some of these techniques. Some concluding discussions are given in Section 6.

2. Theory of 3D imaging and progress of its development

In this section, we describe the fundamentals of ray-based and wavefront-based 3D imaging respectively. It will reveal why 3D imaging with depth measurements becomes a trend.

2.1. Ray-based light field imaging

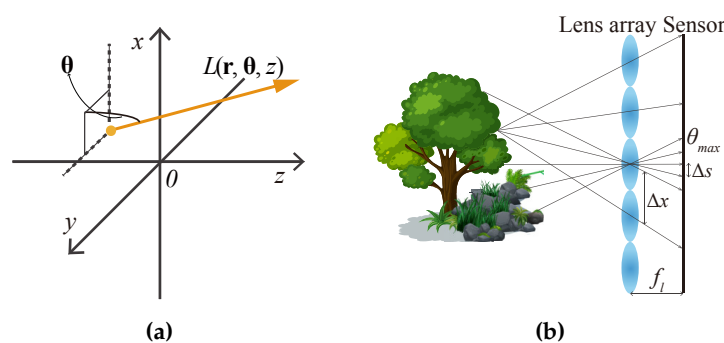


Figure 4. Light field (a) and its conventional capture (b).

As Fig. 4(a) shows, according to the plenoptic function [28], light ray field can be parameterized as a function $L(\mathbf{r}, \theta, z)$ with its spatial position (\mathbf{r}, z) and propagation direction θ , where \mathbf{r} is the position vector representing the transverse spatial coordinates (x, y) and θ is the propagation vector of (θ_x, θ_y) . Because of the conventional capture approach, light ray field is usually expressed by two planes as a four-dimensional (4D) function [29]. In this paper, we use the former one for convenience. Assuming

that the energy traveling along the optical rays is a constant, the 2D images detected by a camera at a plane perpendicular to the optical axis at z_c can be expressed by angularly integrating the light rays

$$\mathcal{I}_i(\mathbf{r}, z_c) = \frac{1}{z_c^2} \int_{-\infty}^{\infty} L(\mathbf{r}, \boldsymbol{\theta}, z_c) d\boldsymbol{\theta}. \quad (1)$$

The light ray field can also be easily propagated from a plane at z to another plane at z' by [30]

$$L(\mathbf{r}, \boldsymbol{\theta}, z') = L\left(\frac{\mathbf{r}}{\alpha} + \boldsymbol{\theta} \left(1 - \frac{1}{\alpha}\right), \boldsymbol{\theta}, z\right), \quad (2)$$

where $z' = \alpha z$, and α is a natural number. The transformation property of the light ray field makes it useful for 3D imaging such as depth map reconstruction [31] and digital refocusing [30,30]. Besides, it is also an efficient way for glass-free 3D displays [13,14,32].

Various light ray field acquisition methods have been developed, including complicated setups such as camera arrays [33,34], compact designs that utilize micro-lens arrays [30,35], frequency domain multiplexing [35], amplitude masks [36,37], and well-designed mirrors [38,39]. Among these techniques, a camera with a micro-lens array in front of its sensor [30,40,41] is well-known and widely used due to its single-shot convenience, as Fig. 4(b) shows. In this kind of capture, every micro-lens captures angular distribution of the light rays at its principal point. The number of light rays that can be recorded depends on the lens pitch Δ_x and the pixel pitch Δ_s of the camera sensor. The maximum angle θ_{max} of the light rays that can be collected depends on the focal length f_l and the lens pitch Δ_x . The spatial sampling interval of the object is the same as the pitch of the lens array. This lens array based method enables direct capture of the light field at a single shot, but the spatial resolution and angular resolution of the captured light field mutually restrict each other [13,14]. This mutual restriction occurs in the similar setups like camera array. During the past 15 years, many techniques have been proposed to enhance the spatial resolution, the view angle and the expressible depth range [14,42–44]. Unfortunately, there is no way to eliminate these shortages that inherited from the array-like devices.

Based on the fact that depth measurements carry the 3D information of the objects, researchers have tended to retrieving light ray field from depth measurements instead of using arrays. We review these techniques in Section 3.

2.2. Wavefront-based light field imaging

Wavefront-based light field imaging can mainly be categorized into two types, the interferometric approach and phase retrieval. The early wavefront light field imaging is based on the interferometry of waves, generally known as holography, which was first invented for microscopic imaging by Dennis Gabor [22] in 1948. As Fig. 5(a) shows, the interference between the object wave and a known reference wave converts the object wave phase into intensity modulation, which makes it possible to reconstruct the phase both optically [45,46] and digitally [23,47]. However, introducing a reference beam requires a complicated interference experimental setup, which limits its applications and also induces some other problems in hologram reconstruction, such as the direct current (DC) term, twin-image, and speckle noise. Solving these problems usually requires a more complicated experiment setup [46,48,49]. Therefore, interferometric techniques are not well suited to imaging, such as an optical microscope that requires partially coherent light. It is necessary to remove the complexity and the coherent limitations of the interferometric techniques. Alternatively, this can be achieved by using out-of-focus images. We can use one intensity image measured with a known complex transfer function or a set of out-of-focus intensity images to estimate the phase quantitatively. This is known as phase retrieval. It takes the advantage of the development of computational imaging [17], leading to a versatile and simple experimental imaging system. Even optical components like lenses are non-essential in a phase

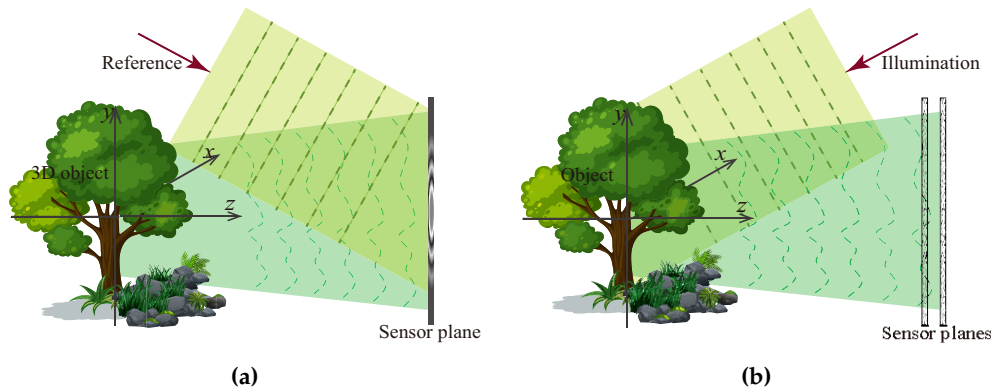


Figure 5. Two typical wavefront imaging techniques: interferometric (a) and phase imaging (b).

imaging setup with depth measurements, as Fig. 5(b) shows, which leads to a broader applications of phase imaging, such as X-ray imaging [50].

Phase retrieval usually can be achieved by iterative and quantitative approaches. Both only require one or a few depth measurements of the diffracted wave. In Section 4, we will review this kind of techniques.

3. Ray-based light field imaging from depth measurements

In light ray field reconstruction, the depth measurements are usually detected by a conventional camera such as a digital single-lens reflex (DSLR), under white light source. The formation of the photographic images has a close connection to the light ray field under geometric optics, and we will show this in the following paragraphs. After this, we will review the related techniques.

3.1. Focal sweeping measurement with a conventional camera

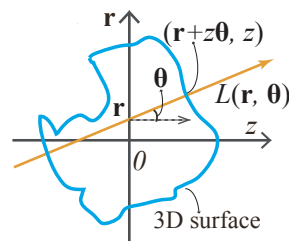


Figure 6. A 3D object's light field representation.

We start from considering a 3D object with its center located at the origin of the Cartesian coordinates. Suppose the center of the 3D object $\mathcal{O}(\mathbf{r}, z)$ is located at the origin of the coordinate system, and it is regarded as a stack of 2D slices, i.e., $\mathcal{O}(\mathbf{r}, z) = \int \mathcal{O}(\mathbf{r}, z)$. The light ray field representation of the 3D object with the principal plane located at its center can be expressed as the integral of the object's projections by Fig. 6 with [51]

$$L(\mathbf{r}, \theta, 0) = \int \mathcal{O}(\mathbf{r} + z\theta, z) dz. \quad (3)$$

Figure 6 shows the geometry relationship between the 3D object surface and its light ray field on the \mathbf{r} - z sectional plane.

In the focal plane sweeping capturing system, usually, only a camera with no other optical components is used, as Fig. 7 shows. The captured image $\mathcal{I}_i(\mathbf{r})$ is the convolution between the image

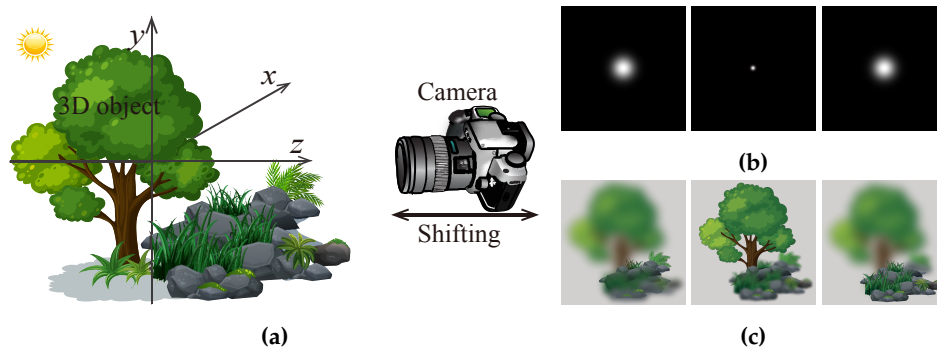


Figure 7. Scheme of focal sweeping capture (a), and sample of the captured images of a point source (b) and a 3D scene (c).

of the object and the point spread function (PSF) of the system at the corresponding plane [52]. Mark $\mathcal{I}_i(\mathbf{r}, z_c)$ as a captured image at a plane of z_c , it thus can be expressed as

$$\mathcal{I}_i(\mathbf{r}, z_c) = \int \mathcal{O}(\mathbf{r}, z) \otimes h_i(\mathbf{r}, z_c - z), \quad (4)$$

where $h_i(\mathbf{r}, z)$ is the PSF of an incoherent imaging system, and \otimes is the 2D convolution operator. Since the aperture of a camera is usually circular, its PSF is approximately a 3D Gaussian distribution function which is symmetrical with respect to the focal plane along the optical axis [53,54]. Figure 7 (b) shows a sample of several simulated 2D slices of the 3D PSF in a conventional camera imaging system, and Fig. 7 (c) shows several sample images captured at different planes.

Because of Eq. (4), the early light ray field reconstruction algorithms from photographic images use image deconvolution, which is an inverse process of Eq. (4) [55]. However, the blur kernel, which is related to the PSF, requires dense sampling to build, and thus could not give good results when the number of samples is limited. Subsequently, techniques involving the insertion of coded masks into a camera have been invented to obtain a higher resolution light ray field [18,56]. Although they achieve a better resolution than the lens array based techniques, they sacrifice light transmission because of the masks. Besides, they usually require solving a computationally intensive inverse problem, often with prior knowledge of the object scene. All of these problems limit their applications [36,57].

In recent years, focal stack imaging has attracted a lot of attention [58]. Focal stack is well known as a tool for extended depth of field photography [59] and fluorescence tomography [60]. Researchers have reported that it is also possible to reconstruct a light ray field from a multi-focus image stack [61–63]. The reason why light ray field can be extracted from a focal stack is obvious, as the 3D information is stored in the stack. This can also be explained mathematically. It is due to the interchangeable property between light ray field and photographic images presented by Eqs. (4) and (1), which is fundamental to most light ray reconstruction techniques that are based on depth measurements. In such techniques, there is no need to mount or insert any additional optical elements to the camera, making it possible to capture a light ray field with commercial DSLR cameras.

To achieve focal plane shifting, we can shift both the camera and the object along the optical axis [62], rotate the focus ring of the camera [27], or modulate the PSF by optical components [64,65]. The camera shift can be controlled digitally [51,66] or mechanically [27,62]. The reconstructed light ray field has a high resolution comparable to the modern camera sensor because the images are not segmented by the sub lens of the lens array. It can also be used for digital refocusing of the scene, synthesizing apertures of arbitrary shapes and sizes, estimating the structure of the scene, and reconstructing the 3D shapes [62,63].

In the following section, we give a review on this kind of techniques, especially the light field reconstruction with back projection (LFBP) approach [62,63] and the light field moment imaging (LFMI) [27,67].

3.2. Light ray field reconstruction by back-projection

Because of the interchangeable relationship between light ray field and 2D photographic images, the light field can be reconstructed from the depth measured photographic images directly by back-projection.

Suppose $\mathcal{I}_i(\mathbf{r}, z_q)$ is a photographic image taken at $z = z_q$, and m is the index number of one image in the photo stack. The total number of captured images is denoted as Q . With these captured images, the light field with the principal plane located at $z = 0$ is calculated by using the back-projection algorithm [62]

$$L(\mathbf{r}, \boldsymbol{\theta}, 0) = \frac{1}{Q} \sum_{q=1}^Q \mathcal{I}_i(\mathbf{r} + z_q \boldsymbol{\theta}, z_q). \quad (5)$$

We call the light ray field reconstruction directly with this equation as LFBP I. Here, we neglect the magnification factor of the images. This is because the captured images can be aligned and resized easily with digital post-processing. Eq. (5) can be explained by Fig. 8 more intuitively. In Fig. 8(a), a light ray $L(\mathbf{r}, \boldsymbol{\theta}, 0)$ with a propagation direction of $\boldsymbol{\theta}$ contributes to two different positions in the defocus images, in front of and behind it, i.e., \mathbf{r}_1 in the front image and \mathbf{r}_2 in the real image. The positions can be obtained by the projection angle and the depth position of these images by $\mathbf{r}_q = \mathbf{r} + z_q \boldsymbol{\theta}$. Based on this fact, the radiance of the light ray can be obtained by the average value of the pixels on all of the depth images along the ray directions.

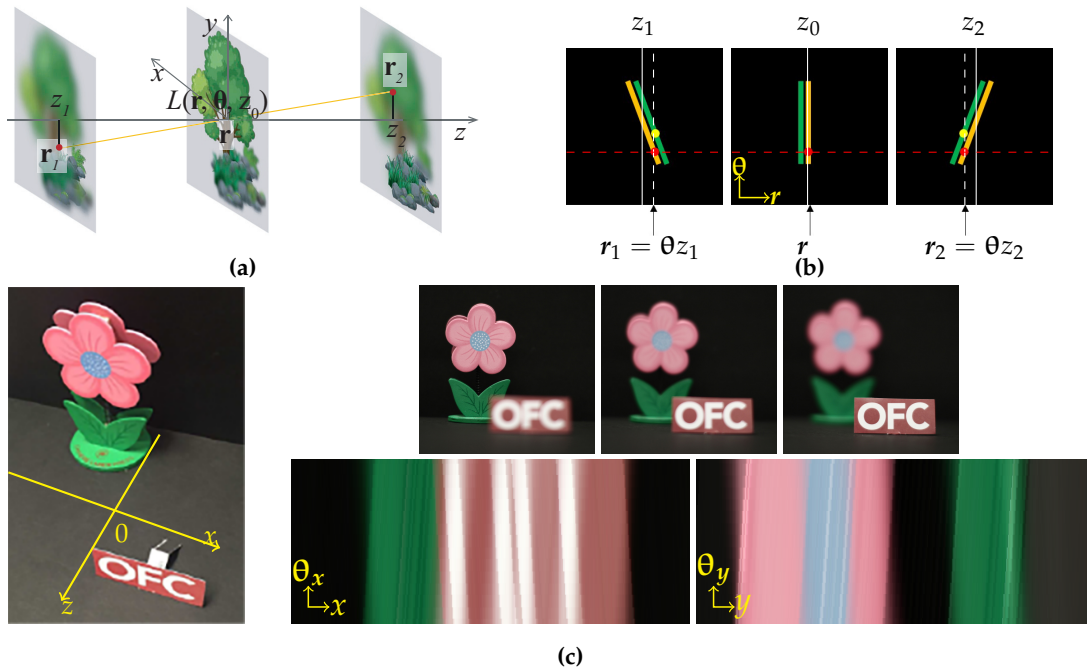


Figure 8. Principle of LFBP represented in the spatial domain (a) and by WDF (b), and an example of the reconstructed EPIs of a real 3D scene (c) (Adapted with permission from [66], [Optical Society of America]).

Figure 8(b) shows the corresponding epipolar plane image (EPI) explanation. Focal plane sweeping in spatial space corresponds to shearing of the EPI, with the degree of shearing reflecting the focal plane sweeping distance [62], in a way similar to the property of the Wigner distribution

function (WDF) [68]. A ray with a fixed propagation angle corresponds to different shearing of the focused EPI, therefore, its radiance can be obtained by integrating over all the red points in the three EPI images, i.e., accumulation along the red dashed horizontal line. Figure 8(c) shows an example of the LFBP I technique, where the left image shows the 3D object scene, and the upper right images are the captured images, whereas the bottom right images are the EPIs of the reconstructed light field. Since the captured images are not segmented by lens arrays, the reconstructed light ray field shows a better angular and spatial resolution, as reflected by the EPIs in Fig. 8(c). The spatial image resolution is comparable to that of a conventional camera sensor. Note that the angular sampling of the light field calculated from the photographic images depends on the numerical aperture (NA) and the pixel pitch of the camera sensor, rather than the number of images captured along the optical axis.

As the EPIs shown in Fig. 8(c), the light field reconstructed with this approach has a severe noise problem [62,66,69]. The EPIs show overlap, and this phenomenon is very serious when the 3D scene is complicated. Chen *et al.* have analyzed this noise by giving the exact expression of the LFBP that relates to the depth measurements [51]

$$L'(\mathbf{r}, \theta) = \sum_{q=1}^Q \mathcal{O}(\mathbf{r} + z_q \theta, z_q) + \sum_{q=1}^Q \int_{z \neq z_q} \mathcal{O}(\mathbf{r} + z_q \theta, z) \otimes h_i(\mathbf{r} + z_q \theta, z_q - z) dz. \quad (6)$$

Since a 3D object $\mathcal{O}(\mathbf{r}, z)$ can be discretized along the optical axis by $\mathcal{O}(\mathbf{r}, z) \approx \sum_{n=1}^N \mathcal{O}(\mathbf{r}, z_n)$, where N is the slice number, Eq. (3) can be rewritten as $L(\mathbf{r}, \theta) = \sum_{n=1}^N \mathcal{O}(\mathbf{r} + z_n \theta, z_n)$. Therefore, when Q in Eq. (6) approaches N , the first term approaches Eq. (3), which corresponds to the discrete approximation of the 3D objects' light field. When Q is much smaller than N , it is equivalent to axially sampling the object insufficiently, which affects the depth resolution of the reconstructed light field. The second term of Eq. (6) is noise. Obviously, it is the accumulation of the defocus noise induced by the images of the object slices which are out of focus. From this equation, we can see that there are two main parameters affecting the noise: the number of depth images and the PSF of the camera. The PSF is related to the f-number of the camera, i.e., the NA. As the second term of Eq. (6) shows, for the LFBP technique, smaller NA and fewer images produce higher quality reconstructed light ray field. However, to maintain the depth resolution of the reconstructed light field, the number of the captured images should be large enough. This mutual constraint property makes it difficult to get a high-quality light field with the conventional LFBP technique. This can be observed from the original paper [62] and the EPIs of Figs. 9(a) and (c).

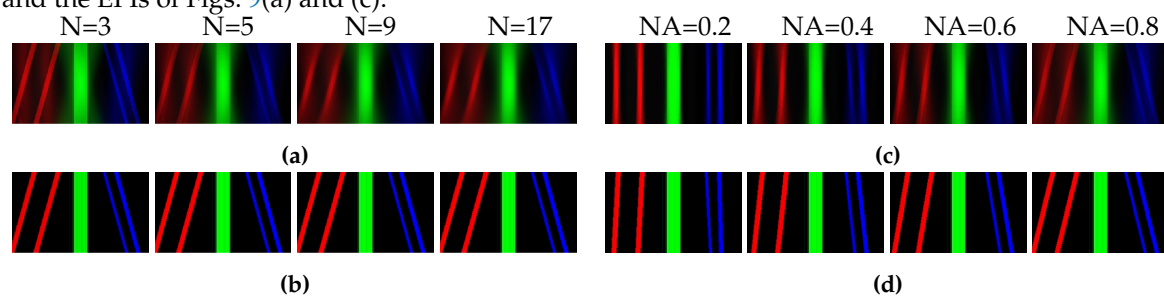


Figure 9. The reconstructed EPIs calculated from various number of depth images (a)(b) and 5 depth images captured under various camera NAs (c)(d), by the conventional LFBP I (a)(c) and denoised LFBP II (b)(d) respectively. (Adapted with permission from [51], [Optical Society of America].)

Based on the fact that (1) each point on the 3D object only focuses at one plane in the depth images, and (2) the largest amount of changes of the depth images indicates the clearest image location, the defocus noise can be eliminated by preprocessing the depth images before light field reconstruction [51]. The quality of the reconstructed light field is improved a lot, as the EPIs shown in Figs. 9(b) and (d). Similarly, more sophisticated depth map calculation algorithm with sequential layered EPI calculation can be applied to achieve more realistic light field reconstruction [63,70]. One method is akin to

restructuring the 3D model firstly, then represent it with Eq. (3). Hence, it is very dependent on the depth map calculation algorithm. For comparison, we name the above two improved LFBP techniques as LFBP II [51,63].

3.3. Iterative light ray field reconstruction based on back-projection

In order to obtain a more realistic light ray field reconstruction with higher quality, iterative light ray field reconstruction based on back-projection (iLFBP) techniques has been reported [71,72]. This kind of techniques are based on the fact of the interchangeable property between 2D camera images and the light ray field, which is indicated by Eqs. (1) and (5). Based on this imaging geometry, both Yin *et al.* and Liu *et al.* have reported an iterative light ray field reconstruction technique from focal stack measurements [71,72]. Their methods share the same concept.

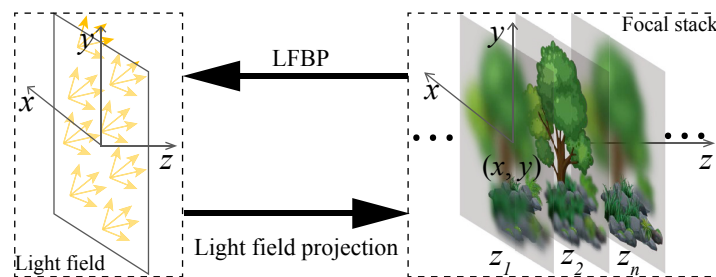


Figure 10. Scheme of iLFBP.

In iLFBP, there is a projection bounce between the 2D focus stack images and the light ray field. For each bounce, a constraint related to the NA of the camera is applied. This is akin to the famous iterative phase retrieval algorithms that we will introduce in Section 4.1. Instead of using the LFBP I, a more sophisticated filtered back-projection algorithm [72] or a Landweber iterative scheme [71] is used to project measured focal stack images to light ray field. This can make the best use of the structural information of the focal stack.

Since this kind of technique does not rely on a preprocessing or the complex nonlinear depth estimation process like in LFBP II, it is not affected by the accuracy of the depth estimation. The experiments show the advantages of this kind of techniques in accuracy, reduced sampling, and occluded boundaries. However, as all the other iterative based techniques, this kind of techniques is heavily time consuming.

3.4. Light field moment imaging

As we illustrated in the previous context, 3D information is carried by the photographic stack images. Even though the light ray field can be reconstructed by LFBP I and LFBP II, the depth resolution is closely related to the axial sampling induced by the depth measurements. Although the iLFBP shows possibility to use fewer images, it still requires quite a lot.

Motivated by the fact of light energy flow along the optical axis is reflected by the sweeping captured images, Orth and Crozier [27] have found that the angular moment of light rays satisfies a Poisson equation:

$$\frac{\partial \mathcal{L}_i(\mathbf{r}, z)}{\partial z} = -\nabla_{\perp} \cdot \nabla U(\mathbf{r}, z) \quad (7)$$

while ∇U is the product of the intensity with the light ray's first angular moment $M(\mathbf{r})$ at the position of (\mathbf{r}, z) , which is determined once being collected by an image sensor, and thus can be calculated from intensity deviation of two [27] or more [67,73] images obtained at different focus distances and

implemented by using conventional cameras. The angular moment is then used to reconstruct 3D perspective views of a scene by [27]

$$\begin{aligned} L(\mathbf{r}, \boldsymbol{\theta}, z) &= \mathcal{I}_i(\mathbf{r}, z) \exp \left\{ -\frac{[\boldsymbol{\theta} - \mathbf{M}(\mathbf{r})]^2}{\sigma^2} \right\} \\ &= \mathcal{I}_i(\mathbf{r}, z) \delta[\boldsymbol{\theta} - \mathbf{M}(\mathbf{r})] \otimes G(\boldsymbol{\theta}, \sigma), \end{aligned} \quad (8)$$

where $G(\boldsymbol{\theta}, \sigma)$ is the Gaussian function with standard deviation σ , which equals to the NA of the system. This is based on the fact that the angular of the light rays satisfy Gaussian function [27], and can be modified properly when the camera used in the capture has a different aperture shape.

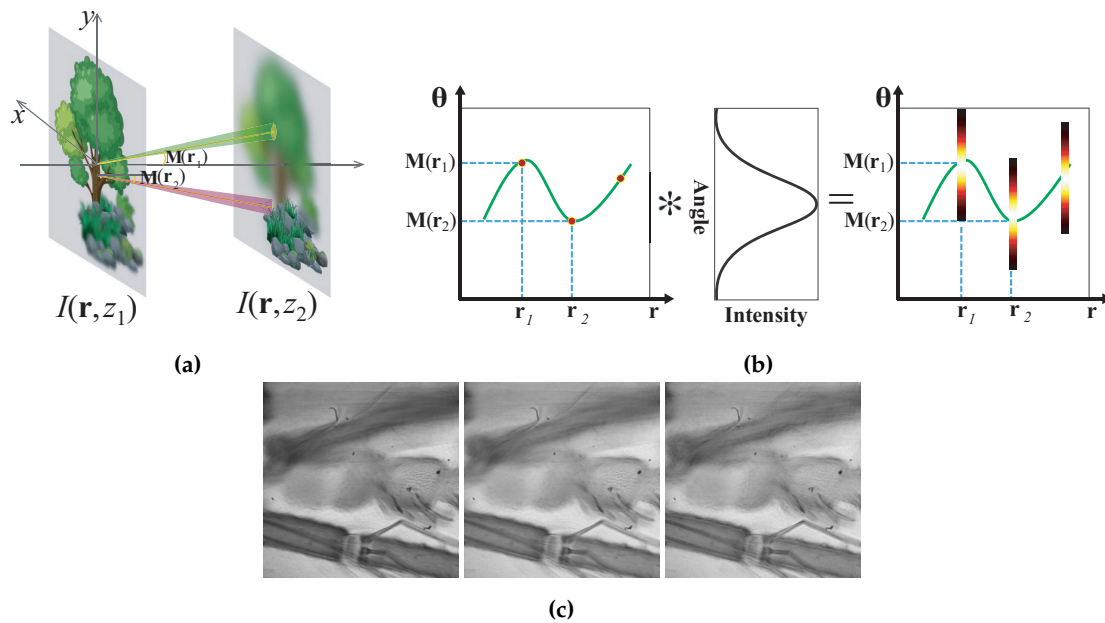


Figure 11. Principle of LFMI represented in the spatial domain (a) and WDF (b), and one example of different view images reconstructed by it (c) (Adapted with permission from [64], [Optical Society of America]).

The theory of LFMI can be explained more intuitively by Fig. 11. Fig. 11(b) represents the LFMI calculation process in one dimensional (1D) EPI expression. The estimated angular moment represents the average light ray propagation direction at each spatial position, as shown in Fig. 11(a), thus can be represented as a curve in 1D EPI, as the left image in Fig. 11(b) shows, which corresponds to $\mathcal{I}_i(\mathbf{r}_n) \delta[\boldsymbol{\theta} - \mathbf{M}(\mathbf{r}_n)]$ in Eq. (8). The final calculated EPI (Right image in Fig. 11(b)) is the convolution between the angular moment and the Gaussian PSF (Center image in Fig. 11(b)). It can be seen that the final EPI is mainly determined by the angular moment, whose accuracy affects the reconstructed light field the most.

LFMI has a counterpart in the wave-optics regime, the transport of intensity equation (TIE), which is a very effective tool for non-interferometric phase retrieval [74]. The key of LFMI is to obtain the first angular moment by solving a Poisson equation that is similar with TIE [27]. Thus, performance is very critical to the axial spacing between adjacent measurement planes [75,76]. Therefore, this axial spacing should be chosen carefully according to the object's characteristics in order to obtain a good estimation of intensity derivative [27]. The estimation accuracy can be further improved with multiple images [67,73]. This issue is precisely identical to the noise-resolution tradeoff in TIE, which will be discussed in detail in Section 4.2.3

It should also be mentioned that, although LFMI provides a new concept for light ray field reconstruction from depth measurements, it can not reconstruct a complete light ray field, but some

perspective view like images. But it provides a new view on depth measurement based light ray field reconstruction, and is still useful for viewing 3D shape of small objects in some extent. More detailed discussions about the relationship between FLMI and TIE can be found in Section 5.2.

3.5. Issues

Table 1. Comparison of light ray field reconstruction techniques.

	Accuracy	Noise	Occlusion	Time cost
LFBP I ^a	Moderate	High	Exist	Low
LFBP II ^b	Moderate	Low	Exist partial ^e	High
iLFBP ^c	High	Low	Exist less	High
LFMI ^d	Low	High	Exist	Low

^a [62], ^b [51,63], ^c [71,77], ^d [27].
^e Occlusion exist in [51] and does not exist in [63].

In this section, we have introduced techniques of light ray field calculation from a series of depth images. Not being segmented by an array device, the spatial resolution is only limited by the camera NA as in conventional photography. As these methods do not require any special equipments like lens array or code masks, they are easy to be implemented. However, they have their issues. Table 1 shows the comparison of these techniques. LFBP based methods can reconstruct the light ray field with defocus noise [62], which can be reduced by preprocessing [51,63] or iterative approaches [71, 72]. However, iteration makes the digital reconstruction time consuming. LFMI [27] reconstruct view like images by estimating the first angular moment of the light rays instead of exact light ray field with at least only two depth measurements, more exact reconstruction may need more depth measurements [67].

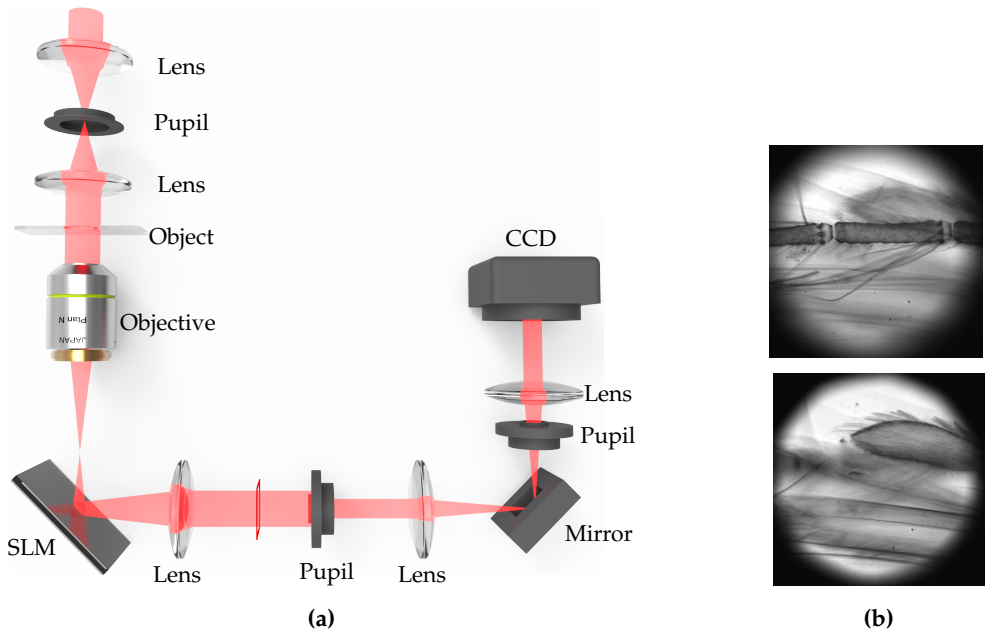


Figure 12. System setup (a) and two of the captured out of focus images (b) of the fast light ray field acquisition with PSF modulation (Adapted with permission from [64], [Optical Society of America].).

The most common problem of the LFBP techniques is the depth resolution that inherits from the depth measurement approach. This requires a large amount of measurements when the object has a large depth. Consequently, this is heavy time consuming and requires fine and stable mechanical alignment in the capture process [51,62,63,72]. Therefore, Wang *et al.* has reported an efficient light-field

acquisition technique by using a spatial light modulator (SLM) to obtain defocussing instead of mechanical translation [64]. This technique can achieve fast data acquisition and is free of mechanical instability. The modulation is implemented in a microscopy imaging system, as Fig. 12 shows. With this system, the time cost for capturing a large amount of focal plane sweeping images is efficiently reduced. And the accuracy of the captured images is increased because there is no mechanical movement during the capture process. This technique may also be used to achieve other types of PSF distribution functions rather than Gaussian. In this case, the Gaussian distribution function in the LFMI equation should be modified to the corresponding PSF function. The microscopic imaging system can also be extended to conventional digital imaging system by using an electrically tunable lens [78] for colorful imaging.

4. Wavefront-based light field imaging from depth measurements

Phase retrieval based wavefront reconstruction techniques does not require any reference beam. Generally, one or several diffracted intensity images and some post digital image processing are needed. This kind of techniques are usually implemented by either iterative or deterministic approaches. Iterative phase retrieval techniques are based on the Gerchberg-Saxton (GS) method [79], and the deterministic approach usually means the TIE [74,80,81]. In the following we review these two types of phase retrieval sequentially.

4.1. Iterative phase retrieval

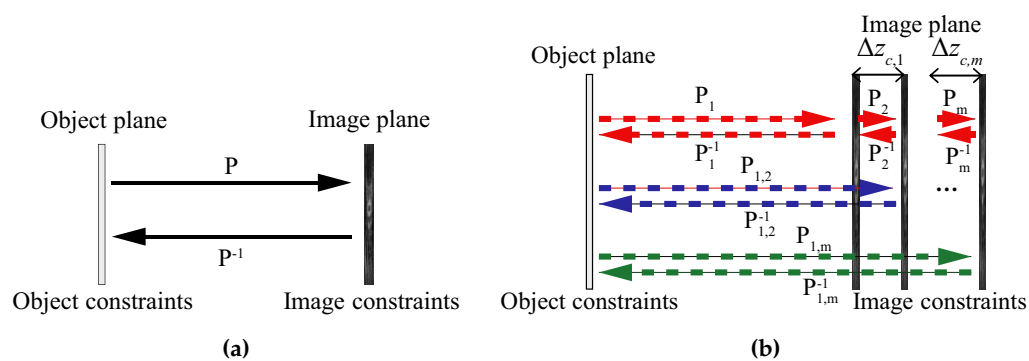


Figure 13. Iterative phase retrieval with (a) one single and (b) multiple depth measurements.

Almost all of the iterative phase retrieval techniques are based on the GS [79] and Yang-Gu (YG) [82] algorithms, which use prior knowledges of the object as constraints [19]. In the GS method, bounces between in-focus and Fourier domain images are performed, as shown in Fig. 13(a), P and P^{-1} is a pair of wave propagation operators. At each step, an estimation of the complex-field is updated with measured or a priori information of the object [19,83,84]. In this case, the accuracy of the phase retrieval is an issue. Phase solutions with this techniques are not unique, but are likely to be correct [85]. Besides, the stagnation of the iteration, and the local minimal problem have limited its application. Many techniques have been proposed for lessening the solution error [86] since this technique was invented.

Fresnel transformed images can also be used instead of Fourier transformed images [87], i.e., P and P^{-1} can be either Fourier transform or Fresnel Transform. The Fresnel transformation between the object and measurement planes instead of Fourier transform was a milestone. This makes the iterations not only be confined between object and image plane, but among multiple diffracted intensity images. The iteration among the object and the measurements can have many combinations, as Fig. 13(b) shows. Bounces can be performed for all of the planes in one loop through the path of $P_1 \rightarrow P_2 \cdots P_m \rightarrow P_m^{-1} \cdots P_2^{-1} \rightarrow P_1^{-1}$, or only be performed between object plane and each image plane sequentially through the path of $P_1 \rightarrow P_1^{-1} \rightarrow P_2 \rightarrow P_2^{-1} \cdots P_m \rightarrow P_m^{-1}$. It can even be

performed only among the measurements. As a result, the prior knowledge about the object became unnecessary. Multiple measurements have improved the accuracy of the phase retrieval and the unnecessary object prior requirement, result in a broader application of iterative phase retrieval [88,89].

In the past decades, research about the iterative algorithm, defocus of the measurements, light modulation, multiple measurements have been fully studied. Fienup has reported the gradient decent search (GDS) algorithm and hybrid input-output (HIO) algorithm successively [19], where the IO has been proved to be very effective and is widely used up to now.

Except improvement on the algorithm, the required properties of the measurements, which represent the image constraints have also been studied. It has been demonstrated that the accuracy of the phase reconstruction is affected by the defocus amount of the measured images [87,90], which is object-dependent. Large propagation distance usually produces better diffraction contrast, thus makes these techniques work better for X-ray imaging [91,92]. A known illumination pattern used as a constraint can eliminate the prior knowledge requirement [89]. A random amplitude mask [93] or random phase plate [94,95] used to modulate the illumination, requires less iterations for reconstruction because the low frequencies of the object are transformed to fast varying high frequencies. The induced problems by these techniques are, an amplitude mask resulting in the diminution of light energy and the use of a phase plate requires difficult fabrication.

Multiple measurements can also be regarded as improving of the object constraint to some extent. Because multiple measurements with variations in depth detect spatial frequencies at different sensitivities [88,96–99], thus they can also improve the resolution of the reconstruction. Multiple depth measurements can be produced by capturing intensity images under illumination with different wavelengths at a single position [100], or under a single beam illumination with different foci [88], translating an aperture transversely [96]. Except for depth measurements, other types of multiple measurements, such as off-axis multiple measurements of synthetic aperture (SA) [101,102], ptychographic [101–104], and structured illumination [105,106] have been proven more efficient in image quality.

The significant amount of the data carried by multiple measurements makes the phase retrieval very robust and rather stable to noise [50]. It is obvious that more measurements result in higher quality reconstructions [107]. However, capturing more intensity images requires more movement steps of the camera or the object, which makes the captured images sensitive to small misalignments in the experimental setup, thus the noise induced to the captured intensity images becomes more serious. Besides, time consuming of the capture makes it not capable for use in dynamic object or real-time applications. To improve the multiple measurement capture [98], beam splitters [50], SLM [108,109], and deformable mirror (DM) [110] were used to achieve single-shot/single-plane measurements. However, beam splitter causes light attenuation, and the use of SLM or DM sacrifices the simplicity of the experimental setup. All of these approaches require additional optical components and involve complicated post digital processes. Therefore, algorithms based on multiple measurements have also been developed on the other hand [99].

The typical iterative phase retrieval techniques are summarized in Table 2. Despite of the limitations of each technique, the iterative phase retrieval remains as a popular technique for wavefront reconstructions due to the fact that the optimal transfer function is object-dependent and the simplicity of its implementation. However, iterative phase retrieval based on scalar diffraction theory [52] works under coherent illumination, which limits its application. TIE, which is presented in the next section of 4.2, has been proved as a compensation to iterative phase retrieval technique.

4.2. Transport of intensity equation

Another important non-interferometric single-beam phase retrieval approach is called TIE. It was originally derived by Teague [21] from the Helmholtz equation under paraxial approximation more than 30 years ago, when its main application fields were adaptive optics [111], transmission electron microscopy (TEM) [112], X-ray imaging [113] and neutron radiography [114]. Recently, technological

Table 2. Comparison of iterative phase retrieval techniques

	Techniques	Pros	Cons
Algorithm	GS	2 images	Error Stagnation Local minima
	GDS	Moderate fast	low
	IO	Effective	
Contraints	Amplitude mask	Fewer iteration	Attenuation
	Phase mask	Fewer iteration	Fabrication
	Known pattern	Fewer iteration	
	Multi-depth	Resolution Single position/shot possible	Time cost Possible experimental complexity
	Multi-wavelength	Resolution Single position	Time cost Expensive
	Multi-angular	Resolution	Experimental complexity
	Structure illumination	Resolution	Experimental complexity
	Synthetic Aperture	Resolution	Experimental complexity

advancements in optical microscopy and digital signal processing have brought TIE back to the forefront of quantitative phase microscopy [115–118] and 3D depth imaging [27,64,119]. The TIE specifies the relationship between object-plane phase and the first derivative of intensity with respect to the optical axis in the near Fresnel region, yielding a compact equation which allows direct recovery of phase information [21]

$$-k \frac{\partial \mathcal{I}(\mathbf{r})}{\partial z} = \nabla \cdot [\mathcal{I}(\mathbf{r}) \nabla \phi(\mathbf{r})], \quad (9)$$

where k is the wave number $2\pi/\lambda$, \mathbf{r} is the position vector representing the transverse spatial coordinates (x, y) . ∇ is the gradient operator over \mathbf{r} , which is normal to the beam propagation direction z . $\mathcal{I}(\mathbf{r})$ is the intensity, located without loss of generality at the plane $z = 0$, and $\phi(\mathbf{r})$ is the phase to be retrieved. Expanding the right hand side (RHS) of Eq. (9), one obtains

$$-k \frac{\partial \mathcal{I}(\mathbf{r})}{\partial z} = \nabla \mathcal{I}(\mathbf{r}) \cdot \nabla \phi(\mathbf{r}) + \mathcal{I}(\mathbf{r}) \nabla^2 \phi(\mathbf{r}). \quad (10)$$

In the above expression, the first term on RHS is called prism term, which stands for the longitude intensity variation due to the local wavefront slope. The second term on RHS is called lens term representing the intensity variation caused by the local wavefront curvature. It can be seen that TIE links the longitudinal intensity derivative with the slope and curvature of the wavefront which produces the change in intensity as the wavefront propagates.

4.2.1. Solutions to TIE

TIE is a second order elliptic partial differential equation for the phase function, and solving this equation does not appear to be difficult. Supposing $\mathcal{I}(\mathbf{r}) > 0$ within enclosure $\bar{\Omega}$ and with appropriate boundary conditions (defined on the region boundary $\partial\Omega$), the solution to the TIE is known to exist and be unique (or unique apart from an arbitrary additive constant) [80], i.e., the phase $\phi(\mathbf{r})$ can be uniquely determined by solving the TIE with the measured intensity \mathcal{I} and the axial intensity derivative $\partial\mathcal{I}/\partial z$. The TIE is conventionally solved under the so-called “Teague’s assumption” so that the transverse flux $\mathcal{I}\nabla\phi$ is conservative and can be fully characterized by a scalar potential ψ (an auxiliary function):

$$\nabla\psi = \mathcal{I}\nabla\phi. \quad (11)$$

Then the TIE can be converted into the following two Poisson's equations:

$$-k \frac{\partial \mathcal{I}}{\partial z} = \nabla^2 \psi, \quad (12)$$

and

$$\nabla \cdot (\mathcal{I}^{-1} \nabla \psi) = \nabla^2 \phi. \quad (13)$$

Solving these two Poisson's equations is straightforward mathematically, and several numerical solvers have been proposed, such as the Green's function method [21,120], the multi-grid method [121,122], the Zernike polynomial expansion method [123,124], the fast Fourier transform (FFT) method [81,121,124,125], the discrete cosine transform (DCT) method [126,127], and the iterative DCT method [128].

Table 3. Comparison of TIE techniques

Issues	Techniques	Pros	Cons
TIE solvers	Green's function ^a	Theoretical analysis	Computation-extensive, memory-demanding
	Multi-Grid ^b	Simple and fast	Low-frequency noise, only for circular regions, difficult to follow details
	Zernike polynomials ^c	Precisely represent the optical aberration	
	FFT ^d	Fast, easy to implement, incorporate regularization in reconstruction	Imply periodic boundary conditions
	DCT ^e	Fast, inhomogeneous Neumann boundary condition	Rectangular aperture, required to limit FOV
Boundary conditions	Iterative DCT ^f	Inhomogeneous Neumann boundary condition, arbitrarily shaped apertures	Need several iterations
	Homogeneous Dirichlet/Neumann ^g	Easy to apply, can be implemented by different solvers	"Flat" boundary phase
	Periodic ^h	Can be implemented by FFT-based solver	Periodic boundary phase
	Inhomogeneous Dirichlet ⁱ	-	Boundary phase required
	Inhomogeneous Neumann ^j	Can be measured by introducing a hard aperture	-
Phase discrepancy	Picard-type iteration ^k	Can compensate the phase discrepancy	Need 2-4 iterations
Axial derivation	2-planes ^l	Less intensity acquisition	Noise-resolution trade off
	Multi-planes ^m	Higher resolution, better noise tolerance	More measurements

^a [21,120], ^b [121,122], ^c [123,124], ^d [81,121,124,125], ^e [126,127], ^f [128], ^g [129,130], ^h [81,121,124,125], ⁱ [21], ^j [126–128], ^k [131], ^l [21], ^m [132–142]

Despite its mathematical well-possessedness, the rigorous implementation of the TIE phase retrieval tends to be difficult because the associated boundary conditions are difficult to measure or to know as a priori. Figure 14 shows three typical boundary conditions used in TIE solvers: Dirichlet boundary conditions, Neumann boundary conditions, and periodic boundary conditions. Since the phase function is exactly the quantity to be recovered, its value $\phi|_{\partial\Omega}$ (for Dirichlet boundary condition) or normal derivative $\mathcal{I}\partial\phi/\partial n|_{\partial\Omega}$ (for Neumann boundary condition) at the region where boundary cannot be known in advance before taking any measurements. To bypass the difficulty, many researchers have tried to solve TIE directly without explicitly imposing the boundary conditions [124,

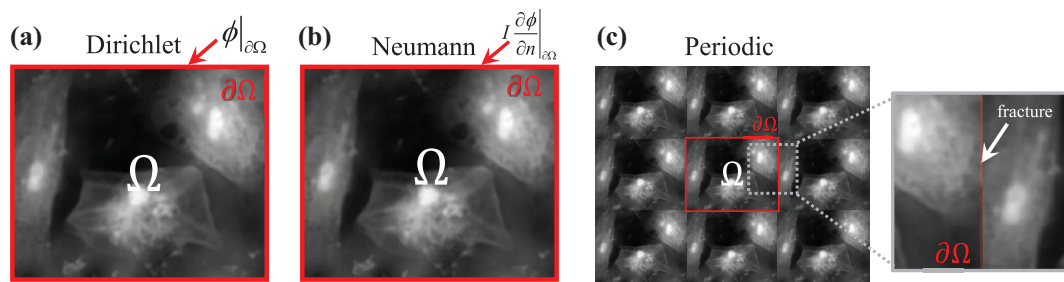


Figure 14. Three typical boundary conditions used in TIE solvers: (a) Dirichlet boundary conditions (need to know the phase value at the boundary), (b) Neumann boundary conditions (need to know the phase normal derivative at the boundary), and (c) periodic boundary conditions (assume the object is periodically extended at the boundary).

[129,130,143]. Coincidentally, all the efforts aim to find some ways to nullify the overall energy transfer across the region boundary, making boundary conditions unnecessary

$$\iint_{\Omega} \frac{\partial \mathcal{I}(\mathbf{r})}{\partial n} d\mathbf{r} = 0. \quad (14)$$

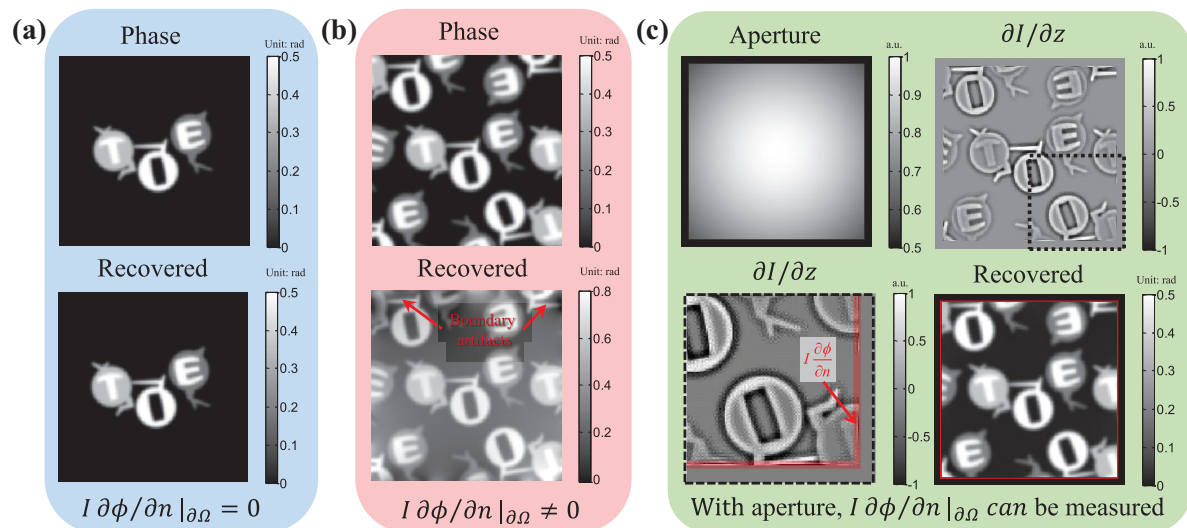


Figure 15. Phase retrieval simulations for different types of objects: (a) An isolated object located in the central FOV (FFT-based solver gives accurate reconstruction), (b) a complex object extending outside the image boundary (FFT-based solver produces large boundary artifacts), and (c) DCT solver with a hard aperture (the inhomogeneous boundary conditions can be measured at the boundary, which produces accurate phase reconstruction even if the object is located at the aperture boundary).

One simple and common way to satisfy this condition is to let the measured sample be isolatedly placed in the center of the camera field of view (FOV), surrounded by an unperturbed plane wave (the phase is “flat” at the boundary of the FOV), in which case the energy (intensity) conservation is fulfilled inside the FOV at different image recording locations, as shown in Fig. 15(a). Then one can safely define some simplified boundary conditions, *e.g.*, the homogeneous Dirichlet conditions (zero phase changes at the boundary $\phi|_{\partial\Omega} = C$, where C is a constant), the homogeneous Neumann boundary conditions (constant phase at the boundary $\mathcal{I}\partial\phi/\partial n|_{\partial\Omega} = 0$), or the periodic boundary conditions (the phase at the boundary repeats cyclically). In this case, the most popular FFT based TIE solver [81,121,124,125,143] works well because it implies periodic boundary conditions due to the cyclic nature of the discrete Fourier transform. Nevertheless, this configuration is rather restrictive and does not reflect general

experimental conditions. When the actual experimental condition violates those imposed assumptions, e.g., in wavefront sensing (non-flat phase at the boundary) or objects extending outside the image boundary, as shown in Fig. 15(b), severe boundary artifacts will appear, and seriously affect the accuracy of the phase reconstruction [129,130,143].

To bypass the difficulty in obtaining real boundary conditions, Gureyev and Nugent [124] suggested another way to eliminate the need of boundary conditions by considering the special case that the intensity $\mathcal{I} > 0$ inside the domain Ω but strictly vanishes at the boundary (so that $\mathcal{I}\partial\phi/\partial n|_{\partial\Omega} = 0$). Alternatively, without any additional requirement about the test object and experimental conditions, Volkov *et al.* [129] proposed a pure mathematical trick to nullify the energy flow across the boundary through appropriate symmetrization of input images. However, it assumes there is no energy dissipation through the image boundary for any objects, which is generally not physically grounded. To summarize, *‘without boundary value measurements’ does not mean that the TIE can be solved without imposing any boundary conditions, or more exactly, we have to confine our measured object or experimental configuration to certain implicit boundary conditions.*

For more general cases, as shown in Fig. 15(b), the energy inside the FOV is not conserved, as energy “leak” occurs at the FOV boundary while the recording distance is being changed. In this case, inhomogeneous boundary conditions are thus necessary for the correct phase reconstruction based on TIE. Zuo *et al.* [126] addressed the solution of the TIE in the case of *inhomogeneous Neumann boundary conditions* under nonuniform illuminations. By introducing a hard aperture to limit the wavefield under test, as shown in Fig. 15(c), the energy conservation can be satisfied, and the inhomogeneous Neumann boundary values $\mathcal{I}\partial\phi/\partial n|_{\partial\Omega}$ are directly accessible around the aperture edge. In the case of *rectangular aperture*, the DCT can be used to solve the TIE effectively and efficiently, which has been well demonstrated in application of microlens characterization [127]. Huang *et al.* [128] further extended the DCT solver to an *arbitrarily shaped aperture* by iterative compensation mechanism. Recently, Ishizuka *et al.* [144,145] successfully applied the iterative DCT solver to recover the additional phase term corresponding to the curvature of field on the image plane in TEM.

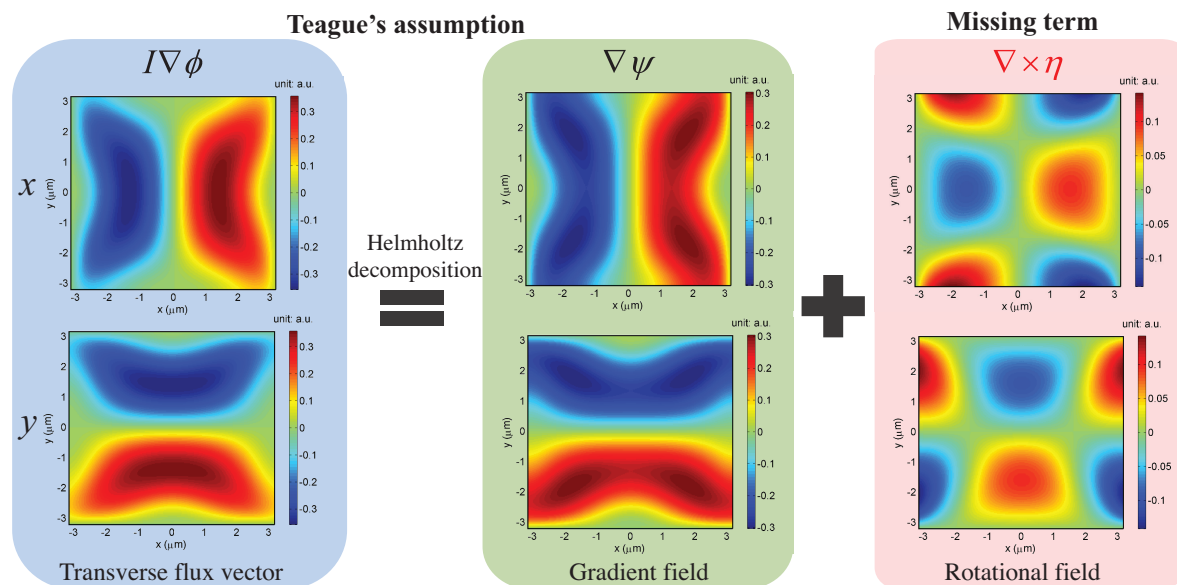


Figure 16. Helmholtz decomposition of the transverse flux field. The x and y components of the vector fields are shown in the first row and the second row, respectively. The term $\nabla \times \eta$ is missing in Teague’s assumption.

4.2.2. Phase discrepancy and compensation

Another notable issue regarding the solution of the TIE is “phase discrepancy” resulting from the introduction of the Teague’s auxiliary function [21], which suggests that the transverse flux is conservative so that a scalar potential ψ exists that satisfy Eq. (11). However, it is important to remark that the Teague’s auxiliary function does not always exist in practical situations since the transverse energy flux may not be conservative, and consequently it would produce results that would not adequately match the exact solution [146]. This problem was first pointed out by Allen *et al.* [121] in 2001. Ten years later, Schmalz *et al.* [146] made a detailed theoretical analysis on this problem based on Helmholtz decomposition theorem and decompose the transverse flux in terms of the gradient of a scalar potential ψ and the curl of a vector potential η :

$$\mathcal{I}\nabla\phi = \nabla\psi + \nabla \times \eta. \quad (15)$$

Compared with Eq. (12), it is plain to see that the term $\nabla \times \eta$ is ignored in Teague’s assumption, making a silent hypothesis that the transverse flux is irrotational (see Fig. 16). In 2014, Zuo *et al.* [131] examined the effect of the missing rotational term on phase reconstruction, and derived the necessary and sufficient condition for the validity of Teague’s assumption:

$$\nabla\mathcal{I}^{-1} \times \nabla^{-2} [\nabla \cdot (\nabla\mathcal{I} \times \nabla\phi)] = 0. \quad (16)$$

Equation (16) shows that if the in-focus intensity distribution is nearly uniform, the phase discrepancy resulting from the Teague’s auxiliary function is quite small ($\nabla\mathcal{I}^{-1} \times \nabla^{-2} [\nabla \cdot (\nabla\mathcal{I} \times \nabla\phi)] \approx 0$). However, when the measured sample exhibits strong absorption, the phase discrepancy may be relatively large and cannot be neglected [146,147]. To compensate the phase discrepancy owing to Teague’s assumption, Zuo *et al.* [131] further developed a simple Picard-type iterative algorithm [131], in which the phase is gradually accumulated until a self-consistent solution is obtained. Within two to four iterations, the phase discrepancy can be reduced to a negligible level, and the exact solution to the TIE can be thus obtained.

4.2.3. Axial intensity derivative estimation

From the previous section, we know that in order to solve the TIE, one need to know the intensity \mathcal{I} and axial intensity derivative $\partial\mathcal{I}/\partial z$. Experimentally, the in-focus intensity \mathcal{I} is easy to obtain. However, the intensity derivative along the optical axis cannot be directly measured. Conventionally, it is estimated by a finite difference between two out-of-focus images, recorded symmetrically about the in-focus plane with $\pm\Delta z$ defocus distances [21], as illustrated in Fig. 17(a).

$$\frac{\partial\mathcal{I}(r)}{\partial z} \approx \frac{\mathcal{I}_{\Delta z}(r) - \mathcal{I}_{-\Delta z}(r)}{2\Delta z}. \quad (17)$$

Mathematically, this approximation is valid in the limit of small defocus distances, where the error is the second order of the focus distance if the data are noise-free. However, experimentally the derivative estimate will become quite unstable when the distance Δz is too small because of the noise and quantization error [137]. On the other hand, increasing the two-plane separation Δz provides better signal-to-noise ratio (SNR) in the derivative estimate, but the breakdown of the linear approximation induces nonlinearity errors, which results in loss of high frequency details [135]. Thus a compromise has to be made where Δz is chosen to balance the non-linearity error and the noise effect [148]. Specifically, the optimal Δz is dependent on both the maximum physically significant frequency of the object and the noise level [148,149]. However, *a priori* knowledge about these two aspects is difficult to be known in advance.

To overcome this trade-off, there has been an increased effort to improve the intensity derivative estimate by utilizing information recorded in multiple defocused planes [132–142]. As illustrated

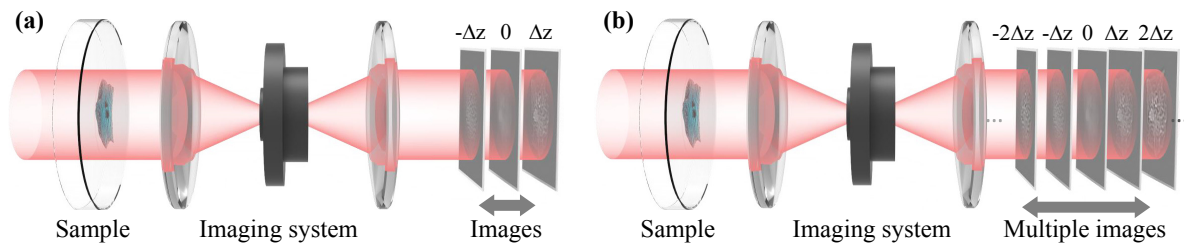


Figure 17. Typical experimental setup for TIE phase retrieval. (a) Conventional 3-plane TIE; (b) Multi-plane TIE. The through-focus intensity stack can be acquired by moving either the object or the image sensor.

in Fig. 17(b), with more intensity measurements $\mathcal{I}_{j\Delta z}(r)$, $j = -n, \dots, -1, 0, 1, \dots, n$, the longitudinal intensity derivative can be represented by their linear combination:

$$\frac{\partial I(r)}{\partial z} \approx \sum_{j=-n}^n \frac{a_j \mathcal{I}_{j\Delta z}(r)}{\Delta z}. \quad (18)$$

Thus, it offers more flexibility for improving the accuracy and noise resistance in derivative estimation. Numerous finite difference methods have been proposed: such as high-order finite difference method [132,134,135,150], noise-reduction finite difference [133,151], higher order finite difference with noise-reduction method [136], and least-squares fitting method [135]. The only difference in these multiple planes derivative estimation methods lies in the coefficients a_j in Eq. (18), and it has been found that all these methods can be unified into Savitzky-Golay differentiation filter (SGDF) [152–154] with different degrees if the finite difference (Eq. (18)) is viewed from the viewpoint of digital filter [137]. Different from these finite difference methods with a fixed degree, methods that decompose the phase in the spatial frequency domain and estimate each Fourier component of the z derivative with an appropriately chosen finite difference approximation are particularly effective because they can balance the effects of noise and diffraction induced nonlinearity over a wide range of spatial frequencies [137–140]. For example, the optimal frequency selection (OFS) scheme proposed by Zuo *et al.* [137], uses a complementary filter bank in spatial frequency domain to select the optimal frequency components of the reconstructed phases based on SGDFs with different degrees to produce a composite phase image. Martinez-Carranza *et al.* [139] extended the idea of multi-filter and frequency selection to accommodate the conventional three-plane TIE solver. Jenkins *et al.* [141] extended the basic principles of the multi-filter phase imaging to the important practical case of partially spatially coherent illumination from an extended incoherent source. Falaggis *et al.* [75] found that the optimum measurement distances obtained by multi-plane phase retrieval form a geometric series that maximizes the range of spatial frequencies to be recovered using a minimum number of planes. This strategy has been successfully implemented in the Gaussian Process regression TIE (GP-TIE) [142] and optimum frequency combination TIE (OFC-TIE) approaches [140], providing high accuracy of phase reconstruction with a significantly reduced number of intensity measurements.

Though multi-plane TIE approaches can solve the trade-off between noise and spatial resolution in conventional three-plane TIE, they require much more intensity measurements at different defocus distances. Manual adjustment or mechanical translation inevitably slow down the data acquisition speed, precluding real-time phase imaging of dynamic process. This issue is basically the same as the one encountered in multi-plane iterative phase retrieval algorithms. Techniques based on multi-wavelength illumination [155,156], electrically tunable lens [78,157], SLM [118,158], and tilted flow cytometry [159] have been reported to yield a fast and tunable focusing scan of the sample, enabling dynamic TIE phase imaging by eliminating the need for any manual or mechanical operations and synchronization of multiple cameras. Furthermore, as shown in Fig. 18 some of techniques [78, 118,157] can be implemented as an add-on module to a commercial microscope, enabling new features

to quantitative phase imaging: diminished speckle effects due to partially coherent illumination, and multimodal investigation potential due to overlaying with other modalities of the microscope (e.g. fluorescence, DIC, phase contrast). More recently, it has been found that the shape of the illumination aperture has a significant impact on the lateral resolution and noise sensitivity of TIE reconstruction [160–163], and by simply replacing the conventional circular illumination aperture with an annular one, high-resolution low-noise phase imaging can be achieved by using only 3-plane intensity measurements [160,161].

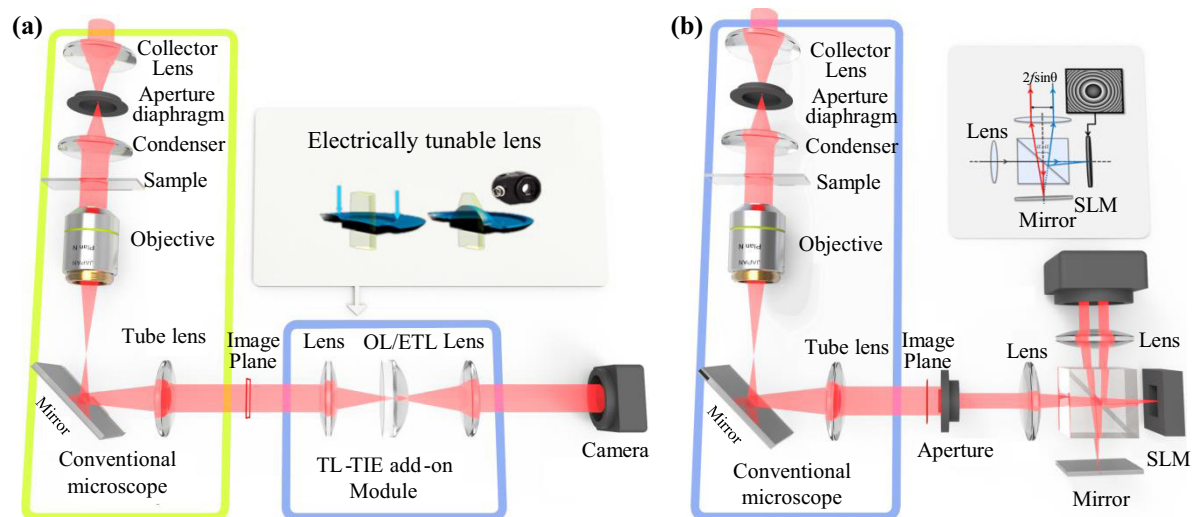


Figure 18. Advanced experimental setups for dynamic TIE phase imaging, which can be implemented as a simple add-on module to a conventional microscope. (a) Electrically tunable lens based TIE microscopy system (TL-TIE, figure adapted with permission from [78]); (b) single-shot TIE system based on a SLM (SQPM, figure adapted with permission from [118]).

4.3. Discussions

Iterative phase retrieval and TIE are both important propagation-based phase imaging techniques, in which the phase contrast is formed by letting the wavefield propagate in free space after interaction with the object. TIE is valid under paraxial approximation and in the limit of small propagation distances (near-Fresnel region). The iterative phase retrieval is less restrictive, which does not rely on paraxial approximation, and is valid for both small and large propagation distances. However, it can sometimes exhibit slow convergence, and stagnation problems described in Section 4.1. TIE is based on solving the intensity transport along the optical wave propagation, which does not explicitly resort to the scalar diffraction theory and does not need iterative reconstruction (deterministic). Besides, it generally requires less intensity measurements than iterative phase retrieval, and can directly recover the absolute phase without requiring phase unwrapping [116,164,165]. Thus, the complexity associated with the 2D phase unwrapping can be bypassed. More importantly, as will be introduced in Section 5.2, TIE is still valid for partially coherent illumination [81,166–169], making it suitable for use in a bright-field microscope [115–118]. However, TIE has its inherent limitations as a tool for quantitative phase retrieval, such as the requirement of small defocus, paraxial approximation, and the inaccurate solutions induced by Teague's assumption and inappropriate boundary conditions.

Combination of the TIE and iterative process has been proved to be particularly effective and able to achieve complementary advantages [155,170–174]. For example, deterministic phase retrieval can be used to provide a "coarse" initial phase, which is then refined by iterative methods, e.g. GS method to recover continuous and discontinuous phase in both near- and far-Fresnel region [155,171,173,174]. Since the TIE reconstructed phase provides a very good initial approximation of the true phase, the

convergence of iterative methods can be significantly improved and the stagnation problems associated with the Gerchberg-Saxton-type iterative algorithm can be effectively avoided.

5. Ray-based vs. wave-based light field imaging

Due to the close connection of the ray and wave optics [8], 3D imaging techniques based on these two theories share many commons. Yamaguchi regards phase of a wavefront as a contribution to the resolution of light ray field [4]. This can be comprehended intuitively from Fig. 2 to some extent. Direction of light rays are along the normal of the wavefront, which is kind of sparse sampling of the continuous wavefront in physical world.

The close connection between wavefront and light rays reflected by many techniques, such as Shack-Hartmann wavefront sensor and light ray field imaging with lens array, the TIE and LFMI. There are also many techniques that take advantage of this fact, such as synthesized hologram from multiple view images [175], hybrid approaches like holographic stereogram [176,177], and 3D Fourier ptychographic microscopy [178]. In the following sections, we show the close connection between wavefront-based and ray-based light field imaging in detail.

5.1. Shack-Hartmann wavefront sensor and light ray field camera

Shack-Hartmann sensor is a well known wavefront sensing technique. In a Shack-Hartmann sensor, a lens array is placed in front of the camera sensor, the intensity images formed in the camera sensor are used to retrieve the income wavefront. Figure 19 shows the structure of the Shack-Hartmann sensor. When a wavefront enters it, there is a focal spot formed on the image sensor behind each individual lenslet. The location of each spot, noted as Δx_n , represents the phase gradient ($\Delta x_n / f_l$) of the wavefront at the corresponding sub-area. The overall wavefront can then be determined by the phase gradient across the entire wavefront.

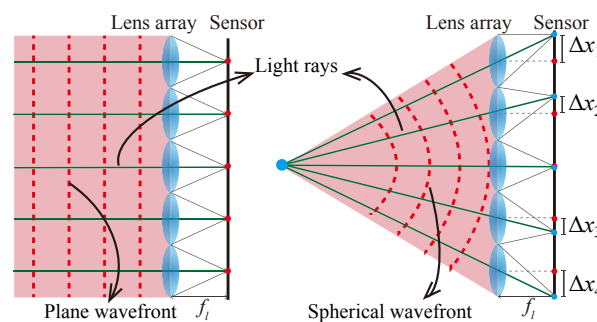


Figure 19. Shack-Hartmann wavefront sensor.

People who are familiar with light ray field imaging with micro lens array [14] can easily find that they share a similar sensing setup: both insert a lens array in front of the camera sensor. This similarity of hardware design comes from the truth that light ray and wavefront are essentially equal to each other. For example, in Fig. 19, the plane wavefront that forms same local point positions in the sensor, like orthographic projection image of light ray field [179]. The spherical wavefront, which introduces different local positions of the point image, is similar to the perspective view images of a point object. The position displacements correspond to view parallax in light field imaging. Ko *et al.* have analyzed the relationship between the Shack-Hartmann sensor and lens let array based light ray field imaging in detail [180]. A comparison under the scenario of wave-optics will be given in the following section.

5.2. Transport of intensity equation and light field moment imaging

As we mentioned in Section 4.2, the TIE was originally derived by Teague [21] from Helmholtz equation under paraxial approximation. However, Teague's TIE as well as his derivation assumes a monochromatic, coherent beam, which might encounter trouble when dealing with wavefields

exhibiting non-negligible partial coherence. Optical coherence theory [8,52] is the formalism used to describe the field in this case, and it is formulated via a description that uses the 2nd order correlation functions of the field, such as the 4D mutual coherence function and cross-spectral density. However, because of the bilinear nature of these quantities, the mathematics become quite complicated and the results are difficult to interpret. As an alternative to the space-time correlation functions, a general coherent or partially coherent optical field can be described in terms of 4D light ray field within geometrical optics, as we introduced in Section 3 [31,181]. The light field has its root in radiometry, representing radiance as a function of position and direction, thereby decomposing optical energy flow along rays. In the geometrical optics picture, a single ray determines neither a field's amplitude nor phase. The surface of the constant phase is interpreted as wavefronts with geometrical light rays travel normal to them, as illustrated in Fig. 20(a). Their directions coincide with the direction of the ensemble/time-averaged Poynting vector, governed by the Eikonal equation within the accuracy of geometrical optics [81,166]. However, from a physical point of view, the ray-based light field representation is not a rigorous model and inadequate to describe interference, diffraction, and coherence effects.

As an effort to bridge wave optics to rays, phase-space distributions such as the WDF have been introduced to the study of partially coherent fields [182]. As illustrated in Fig. 20(b), the WDF describes an optical signal in space and spatial frequency (*i.e.*, direction) simultaneously, and can thus be considered as a counter-part of the radiance (light ray field) in wave optics. It represents the field propagation by a simple geometrical relation, *i.e.*, the WDF is constant under propagation along rays. By allowing the possible negativity, the WDF constitutes a rigorous wave-optical foundation for the theory of radiometry [183]. It is therefore desirable to have a simple mathematical phase-space model for the TIE under partially coherent illumination, providing better understanding of phase retrieval issues by establishing connections between the ray model and more physically correct wave model. Such understanding may lead to further insights to the meaning of the term “phase” of partially coherent fields in such joint context, and facilitate productive exchange of ideas between the fields of TIE phase retrieval and light field imaging.

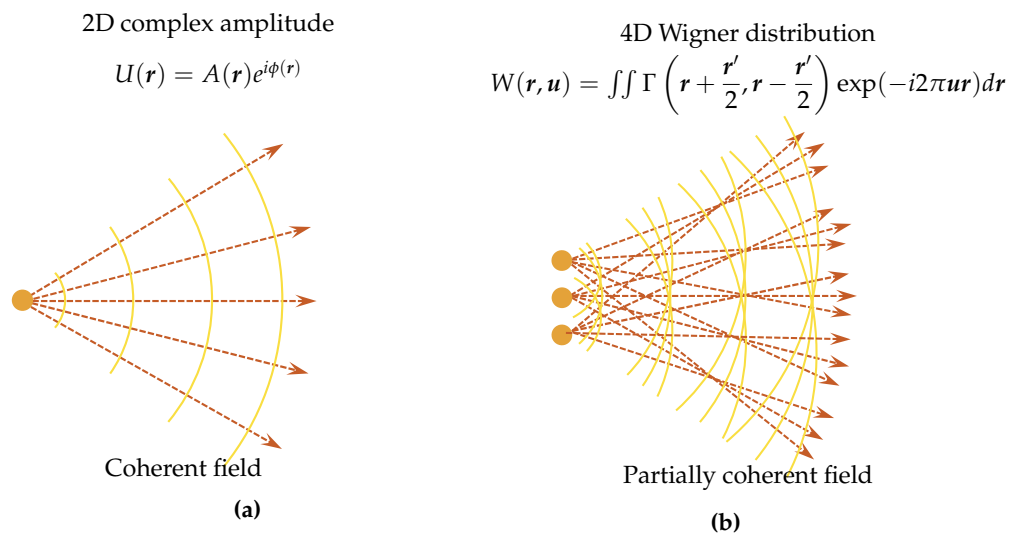


Figure 20. Schematic of a simplistic view of coherent field and partially (spatially) coherent field. (a) For coherent field, the surface of the constant phase is interpreted as wavefronts with geometrical light rays traveling normal to them. It is fully described by 2D complex amplitude. (b) Partially coherent field needs 4D coherence function, like the Wigner distribution, to accurately characterize its properties, like its propagation and diffraction. Besides, partially coherent field does not have a well-defined phase, but rather, a statistical ensemble of phases (spatial frequencies, propagation directions) at every position in space.

5.2.1. Generalized transport of intensity equation (GTIE) for partially coherent field

Since the TIE applied to partially coherent fields reconstructs an only 2D function, it is insufficient to characterize the 4D coherence function [80]. To this end, some variants of the TIE have been reported to account for the partial coherence explicitly. As early as 1984, Streibl [115] extended the Teague's TIE to the general case of partially coherent illumination with the 4D mutual intensity function. He first pointed out the validity of TIE for a spatially partially coherent imaging system, provided that the primary source distribution is symmetric about the optical axis. In 1996, Paganin and Nugent [81] created a meaningful definition of phase for partially coherent fields using the concept of the time-averaged Poynting vector. Gureyev *et al.* [166] described an alternative interpretation with the generalized Eikonal, based on the spectrum decomposition of a polychromatic field. In 2012, Zysk *et al.* [167] further explicitly considered the spatially partial coherence with use of coherent mode decomposition, showing that the phase recovered by the TIE is a weighted average of the phases of all modes. In 2013, Petrucci *et al.* developed a partially coherent TIE based on cross-spectral density, allowing removal of coherence-induced phase inaccuracies [168]. In general, these works clarify the meaning of phase and the validity of TIE under partially coherent illuminations from different perspectives. However, most of these treatments presented here employ conventional space-time correlation quantities, like the mutual intensity and the cross-spectral density function, to describe the properties of the partially coherent light. Though these quantities are adequate for the analysis of the propagation and diffraction with light of any state of coherence, their inherent bilinear, stochastic, and wave-optical nature often leads to complicated mathematics and difficulties in comprehension. In 2015, taking the phase-space theory as the starting point and based on Liouville transport equation [182], Zuo *et al.* derived the generalized TIE (GTIE) for partially coherent field [169]

$$\frac{\partial \mathcal{I}(\mathbf{r})}{\partial z} = -\nabla \cdot \iint \lambda \mathbf{u} \mathbf{W}_{\omega}(\mathbf{r}, \mathbf{u}) d\mathbf{u} d\omega, \quad (19)$$

where \mathbf{u} is the spatial frequency coordinate corresponding to \mathbf{r} . $W_{\omega}(\mathbf{r}, \mathbf{u})$ is the WDF of a given monochromatic component (characterized by the optical frequency $\omega = c/\lambda$, where c is the speed of light and λ is the wavelength) of the whole field. When the field is quasi-monochromatic, i.e., the field can be considered as consisting of single optical frequency, the field can be regarded as almost completely temporally coherent. Thus Eq. (19) reduces to the GTIE for partially spatially coherent fields,

$$\frac{\partial \mathcal{I}(\mathbf{r})}{\partial z} = -\lambda \nabla \cdot \int \mathbf{u} \mathbf{W}(\mathbf{r}, \mathbf{u}) d\mathbf{u}. \quad (20)$$

However, quasi-monochromatic fields still are not necessarily deterministic due to the statistical fluctuations over the spatial dimension. This randomness can be removed by further limiting the field to be completely spatially coherent as well. Then the field becomes deterministic and can be fully described by the 2D complex amplitude $U(\mathbf{r}) = \sqrt{\mathcal{I}(\mathbf{r})} \exp[i\phi(\mathbf{r})]$, where $\phi(\mathbf{r})$ is the phase of coherent field, as shown in Fig. 20(a). From the time(space)-frequency analysis perspective, the completely coherent field can be regarded as a mono-component signal, and the first conditional frequency moment of the WDF (instantaneous frequency) is related to the transverse phase gradient of the complex field [184,185]:

$$\frac{\int \mathbf{u} \mathbf{W}(\mathbf{r}, \mathbf{u}) d\mathbf{u}}{\int \mathbf{W}(\mathbf{r}, \mathbf{u}) d\mathbf{u}} = \frac{1}{2\pi} \nabla \phi(\mathbf{r}). \quad (21)$$

Substituting Eq. (18) into Eq. (17) leads to Teague's TIE

$$\frac{\partial \mathcal{I}(\mathbf{r})}{\partial z} = -\frac{1}{k} \nabla \cdot [\mathcal{I}(\mathbf{r}) \nabla \phi(\mathbf{r})]. \quad (22)$$

Thus, Teague's TIE is only a limiting case of GTIE when the optical field is completely (both temporally and spatially) coherent. The GTIE, in contrast, explicitly considers the coherent states of the field so that it applies to a much wider range of optical- and electron-beams.

5.2.2. Phase-space definition of "phase" for partially coherent field

One difficulty in extending the GTIE to phase retrieval arises from the fact that the partially coherent field does not have a well-defined phase since the field experiences statistical fluctuations over time. However, the phase-space representation on the left hand side (LHS) of Eq. (19) is still valid, leading to a new meaningful and more general definition of "phase". Here we refer to the new "phase" $\tilde{\phi}(\mathbf{r})$ defined by Eq. (21) as the generalized phase of partially coherent fields to distinguish it from its coherent counterpart. It can be seen from Eq. (21) that the generalized phase is *a scalar potential whose gradient yields the conditional frequency moment of the WDF*. It is clear from a distribution point of view that the quantity is the average spatial frequency at a particular location. In the optical context, the simultaneous space-frequency description of the WDF is analogous to what is known as the radiance, which describes the amount of energy each ray carries [183]. Thus, $W(\mathbf{r}, \mathbf{u})$ can be intuitively interpreted as the energy density of the ray travelling through the point \mathbf{r} and having a frequency (direction) \mathbf{u} . The frequency moment of the WDF, $\int \mathbf{u}W(\mathbf{x}, \mathbf{u})d\mathbf{u}$, represents the transversal ensemble/time-averaged flux vector (transversal time-averaged Poynting vector) [185,186]. The ratio of the time-averaged flux vector to the intensity (so called normalized average flux/Poynting vector) gives the time-averaged directions of the energy flow. Thus Eq. (21) suggests that the time-averaged flux lines are defined as the orthogonal trajectories to the generalized phase (or wavefront), they coincide with the direction of the average Poynting vector [81]. However, it should be noted that the WDF is not a rigorous energy density function (radiance function) due to its possibility for negativeness. The negative values of the WDF originate from the phase space interference [187], and can trace back to the uncertainty principle in optics [188], allowing the description of coherent effects, such as interference and diffraction. However, no problems are encountered when the WDF is used to represent other quantities that can be measured. For example, the WDF marginal projections used in Eq. (21), which give measurable quantities (intensity, time-averaged Poynting vector), are always non-negative. Furthermore, in the case of low spatial coherence where coherent interference effects statistically wash out, or a coherent field with a slowly varying wavefront, one can safely interpret the WDF as energy density without worrying about the negativity.

5.2.3. Light field moment imaging using TIE

We have already introduced LFMI, a computational light-field retrieval method, in Section 3. In this section, we establish connections between the TIE phase retrieval and light ray field imaging. Essentially, the two imaging procedures both look for complete descriptions of the properties of a field, but from different perspectives. Light ray field (radiance) represents all possible light rays in the field as a 4D function of position and direction, while for coherent imaging applications, the 2D complex field encodes the position and direction information in its amplitude and phase. The 2D intensity and phase give total knowledge about the complex field so that the behavior of the field can be perfectly predicted. Such complete knowledge permits various forms of coherent optical imaging systems, such as the Zernike phase contrast and differential interference contrast imaging to be computationally emulated without resorting to actual optical hardware [78,160,189,190]. Obviously, the 4D phase-space representation of a coherent field is highly redundant because the complex field is defined only over the 2D plane. This phase-space redundancy leads to a highly localized WDF, but is usually accompanied with oscillations (include negative values) due to the phase-space interference contributions [183,191,192]. For a slowly varying object, the phase-space redundancy becomes more

apparent since the phase-space oscillations disappear (the diffraction effect can be neglected) and the WDF occupies only a single slice in phase space [169]:

$$W(\mathbf{r}, \mathbf{u}) = \mathcal{I}(\mathbf{r}) \delta \left[\mathbf{u} - \frac{1}{2\pi} \nabla \phi(\mathbf{r}) \right]. \quad (23)$$

The form of the WDF given above now is a true energy probability distribution in phase space, telling us the geometric ray or energy flow at single position travels only along single direction described by the phase normal (coincides with the direction of the Poynting vector), as shown in Fig. 20(a) and Fig. 21(a). This is an advantageous feature to allow phase measurement simply by measuring the directions of the rays, *e.g.* the Shack-Hartmann sensor [193]. Figure 21 visualizes a smooth coherent wavefront and its corresponding WDF and light field representation, with the simple relation $\theta = \lambda u$ connecting the spatial frequency and the ray angle.

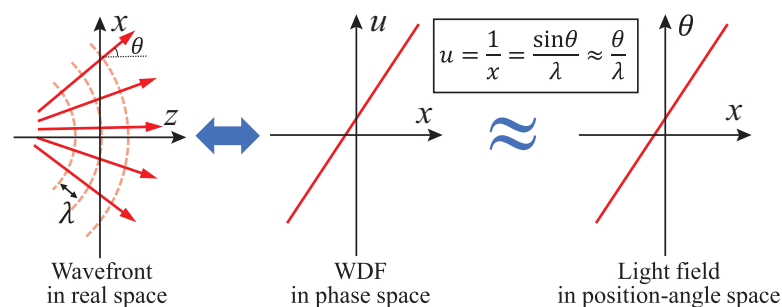


Figure 21. Visualization of a smooth coherent wavefront and its corresponding WDF and light field. The phase is represented as the localized spatial frequency (instantaneous frequency) in the WDF representation. Rays travel perpendicular to the wavefront (phase gradient).

The situation becomes more complex when the field is not strictly coherent. Generally, the phase-space WDF constitutes a rigorous and non-redundant description for partially coherent fields. The knowledge of amplitude and (generalized) phase are not sufficient to determine the full field unambiguously [80,194]. The complete characterization of the 4D coherence function (so-called coherence measurement or coherence retrieval) has always been an active research area. The representative approaches include direct interferometric measurement [195,196], phase-space tomography [197,198], multi-plane coherence retrieval [199,200], are windowed Fourier transform approach [201,202].

If the field exhibits significant spatial incoherence, the negativity and oscillations problem in WDF can be significantly reduced or even disappears, and then the WDF again approaches to the radiance or the light field. From the geometric optics perspective, for each point on the beam there exist many geometric rays with different directions, and they fan out to make a 2D distribution, which accounts for the higher dimensionality of the partially coherent field, as illustrated in Fig. 22(b). The light field camera, as a counterpart of the Shack-Hartmann sensor in the computer graphics community, allows joint measurement of the spatial and directional distribution of the incoherent light field [30,203]. Light ray field imaging enables us to apply ray-tracing techniques to compute synthetic photographs, depth estimation, flexibly change the focus and perspective view[41,203]. However, it requires elaborate optical setups and significantly sacrifices spatial resolution (traded for angular resolution) as compared to conventional imaging technique.

We now consider the potential connections between the TIE phase retrieval and light field imaging. As is shown by Eq. (21), the (generalized) phase of the field (regardless its state of coherence), which is a scalar potential whose gradient yields the conditional frequency moment of the WDF, can be retrieved from the TIE with a minimum of two closely-spaced intensity measurements. Applying the

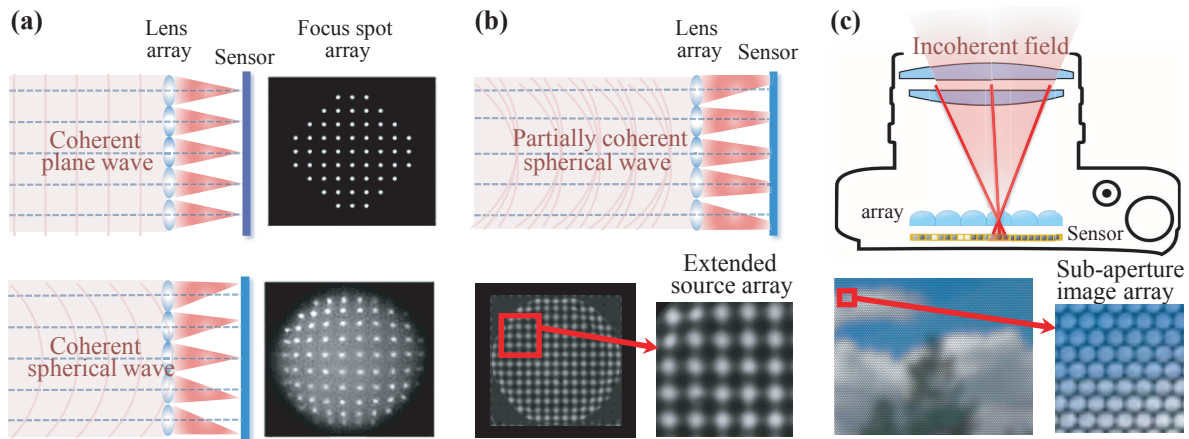


Figure 22. Principle of the Shack-Hartmann sensor and light field camera. (a) For coherent field, Shack-Hartmann sensor forms a focus spot array sensor signal. (b) For partially coherent field, Shack-Hartmann sensor forms an extended source array sensor signal. (c) For incoherent imaging, light field camera produces a 2D sub-aperture image array.

correspondence between WDF and light field, i.e., $L(\mathbf{x}, \boldsymbol{\theta}) \approx \mathbf{W}(\mathbf{r}, \lambda \mathbf{u})$ to Eq. (21), we can describe the phase in terms of the light field:

$$\frac{\int \boldsymbol{\theta} L(\mathbf{r}, \boldsymbol{\theta}) d\boldsymbol{\theta}}{\int L(\mathbf{r}, \boldsymbol{\theta}) d\boldsymbol{\theta}} = k^{-1} \nabla \phi(\mathbf{r}). \quad (24)$$

This equation shows that the phase gradient is related to the normalized transverse average energy flux vector. The well-defined energy flux density vectors are weighted and averaged at a single location to form a unique and also well-defined average flux vector. Put simply, the quantity on the LHS of Eq. (24) is just the centroid of the light field - the average direction of light at one given position. Based on Eq. (24), Zuo *et al.* [169] proposed and verified two important conclusions: (1) 4D light field contains 2D (generalized) phase information (phase can be recovered by analyzing the light field image): the phase gradient can be easily recovered from the 4D light field by a simple centroid detection scheme, which is similar with the standard procedure in the Shack-Hartmann method [193]. The only possible difference is that for coherent wavefronts, geometrical light ray at single position travels only along single direction, so the Shack-Hartmann sensor forms a focus spot array sensor signal, as illustrated in Fig. 22(a). For partially coherent fields, geometric rays at a single position travel in various directions, forming a 2D extended source array instead, as shown in Figs. 22(b). For complete incoherent light field imaging, the ray at one given position travel to all possible directions, producing sub-aperture image array in the image sensor, as illustrated in Fig. 22(c). (2) Though in general a standard TIE measurement cannot recover the complete 4D light field, the retrieved phase provides important information about the light field (its first angular moment). Furthermore, for some simplified conditions (*e.g.* a slowly varying/non-scattering/spread-less specimen under spatially stationary illumination), the 4D light field is highly redundant (as shown in Fig. 23, when the specimen is spreadless, it does not change the angular distribution of the incident field (no scattering, only refraction), which is fully determined by the source intensity distribution, but the direction of each incident ray is shifted as a function of the phase gradient of the object. That is why in Fig. 22(b), the Shack-Hartmann sensor forms an extended source array sensor signal. Thus, with the knowledge of the source intensity distribution (angular distribution of the light field) and the phase of the object $\phi(\mathbf{r})$ retrieved from the TIE, the 4D light field can be fully characterized.

As we introduced in section 3 [27], LFMI is an example of applying the idea of TIE to realize light ray field imaging. It has been proven that the partial differential equation used in LFMI (Eq. 7)

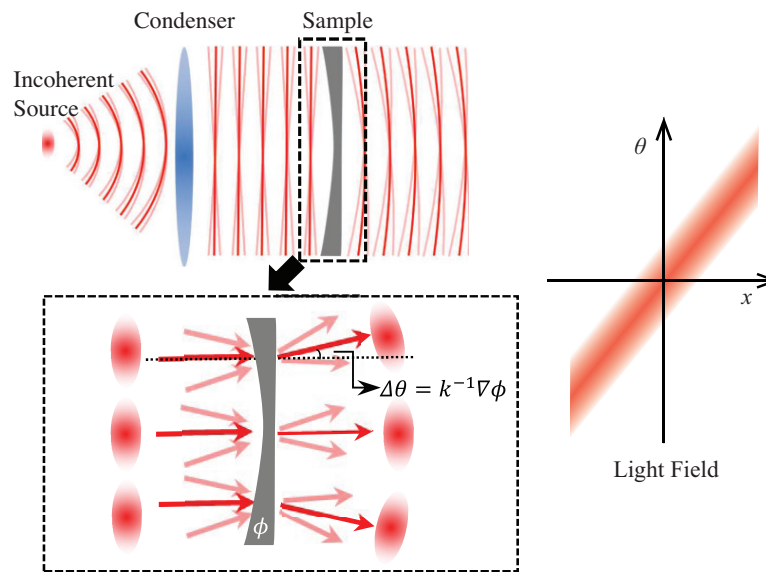


Figure 23. Light field representation of a slowly varying object under spatially stationary illumination. The sample exhibits angle-shift invariance: at each location, the direction of each incident ray shifts by the amount of object phase gradient.

is a variant of TIE at the geometric optics limit [119]. Therefore, any TIE solvers and axial derivative estimation approaches can be applied to LFMI. For example, in 2015, Liu *et al.* [67] adopted the high-order finite difference method to optimize the axial derivative estimation, improving the image quality and signal-to-noise ratio of LFMI. As we mentioned earlier, the phase retrieved by TIE can only be used to reconstruct the first angular moment of the 4D light field, which is exactly the physical meaning of “moment” in LFMI.

5.3. Hologram Synthesis from focal stack measurements

The essential equivalence of light wavefront and ray field allows the interchangeable compatibility between them. Hologram synthesis from light ray field [66,204,205] gets benefits from this fact. This lets holographic imaging enable a break-through the interferometric requirement, and makes hologram of real world more practical. On the other hand, 2D hologram can be used to store 4D light ray field, and makes fast transfer of it be possible, which is of great concern for the light ray field based free-glass 3D display broadcast [13].

Except holographic stereogram [177] and synthesizing hologram from light ray field [66,175,204,205], obtaining hologram from depth measurements has also been proved possible. Not surprisingly, it has been proven that a Fourier hologram $H(u, v)$ can be synthesized directly from depth measured photographic images with [53,54]

$$H(\rho) = \frac{\sum_{q=-Q}^N \Im [\mathcal{I}_i(\mathbf{r}; q\Delta z_i)] \exp \left\{ -j \frac{\pi q \Delta z_i}{\lambda f^2} \rho^2 \right\}}{\sum_{q=-Q}^Q \Im [h(\mathbf{r}; q\Delta z_i)] \cos \left\{ \frac{\pi q \Delta z_i}{\lambda f^2} \rho^2 \right\}}, \quad (25)$$

where ρ is the coordinate of the Fourier spectrum plane, $2Q + 1$ is the number of depth measurements, and Δz_i is the depth interval between two adjacent measurements. \Im is the Fourier transform operator, λ is the wavelength used in hologram synthesizing, and f is the focal length of the virtual Fourier

lens. Eq. (25) has been proven to be equivalent to the Fourier hologram representation of a 3D object $\sum_{n=1}^N \mathcal{O}(x, y, n\Delta z)$ [52] which can be reformed to

$$H(\rho) = \sum_{n=1}^Q \exp \left\{ -j \frac{\pi n \Delta z}{\lambda f^2} \rho^2 \right\} \int \mathcal{O}(r; n\Delta z) \exp \left\{ j \frac{2\pi}{\lambda f} r \rho \right\} dr. \quad (26)$$

In this case, the measurements should cover the whole object space along the optical axis. As the issues in light ray reconstruction from depth measurements, the hologram synthesis shows the same problem, which needs further investigation. This kind of issues also happen in the hologram synthesizing from light ray field [43,204].

6. Conclusions

In this paper, we reviewed 3D imaging techniques that are based on depth measurements. Due to the difference of light sources and the imaging characteristics, they have different applications. The wavefront-based 3D imaging, is more efficient for surveying micro details, thus well applied in microscopy [12] and medical applications. The light rays are a more sparse sampling of the light field, therefore it is usually used for macro applications, such as displays [13]. However, the essential equivalence and close connection of the two have a mutual beneficial relationship, make them interchangeable, and share computational algorithms and hardware concepts. This mutual beneficial relationship also results in combination of them, for example, light ray field can be properly combined with wavefront technique for broader applications and better imaging performance [178].

Even though there is no perfect technique for achieving good imaging quality (resolution, noise), time cost and system complexity at the same time, we are on a progress. Proper techniques depends on the application.

Funding: This work was supported by the Brain Korea 21 Plus Project in 2018.

Acknowledgments: Ni Chen appreciates the financial support from National Natural Science Foundation of China (NSFC) under contract 61705241, Natural Science Foundation of Shanghai (NSFS) under contract 17ZR1433800, and the framework of international cooperation program managed by National Research Foundation of Korea (Young Scientist Program between Korea and China). Chao Zuo appreciates the financial support from NSFC (61722506, 61505081, 11574152), Outstanding Youth Foundation of Jiangsu Province, China (BK20170034), and the Key Research and Development Program of Jiangsu Province, China (BE2017162). We appreciate investigation work of Mr. Haichao Wang (Shanghai Institute of Optics and Fine Mechanics, Chinese Academy of Sciences) and the 3D schematics of optical systems drawn by Mr. Junyi Ding (Nanjing University of Science and Technology, Jiangsu, China).

Author Contributions: B. Lee and N. Chen organized the contents, N. Chen wrote Sections 1, 2, 3.1, 4.1, and 4.3; C. Zuo wrote Sections 4.2, 4.3 and 5.2; All of the authors edited the final paper.

Conflicts of Interest: The authors declare no conflict of interest.

References

1. Google Scholar.
2. Watanabe, T.M.; Sato, T.; Gonda, K.; Higuchi, H. Three-dimensional nanometry of vesicle transport in living cells using dual-focus imaging optics. *Biochemical and Biophysical Research Communications* **2007**, *359*, 1–7. doi:10.1016/j.bbrc.2007.04.168.
3. Tanida, J.; Kumagai, T.; Yamada, K.; Miyatake, S.; Ishida, K.; Morimoto, T.; Kondou, N.; Miyazaki, D.; Ichioka, Y. Thin observation module by bound optics (TOMBO): concept and experimental verification. *Applied Optics* **2001**, *40*, 1806–1813. doi:10.1364/ao.40.001806.
4. Yamaguchi, M. Light-field and holographic three-dimensional displays. *Journal of the Optical Society of America A* **2016**, *33*, 2348–2364. doi:10.1364/josaa.33.002348.
5. Martínez-Corral, M.; Javidi, B. Fundamentals of 3D imaging and displays: a tutorial on integral imaging, light-field, and plenoptic systems. *Advances in Optics and Photonics* **2018**, *10*, 512–566. doi:10.1364/aop.10.000512.

6. Bruning, J.H.; Herriott, D.R.; Gallagher, J.E.; Rosenfeld, D.P.; White, A.D.; Brangaccio, D.J. Digital Wavefront Measuring Interferometer for Testing Optical Surfaces and Lenses. *Applied Optics* **1974**, *13*, 2693. doi:10.1364/ao.13.002693.
7. Wolf, E. Three-dimensional structure determination of semi-transparent objects from holographic data. *Optics Communications* **1969**, *1*, 153–156. doi:10.1016/0030-4018(69)90052-2.
8. Born, M.; Wolf, E. *Principles of Optics*, seven ed.; Cambridge University Press, 1999. doi:10.1017/cbo9781139644181.
9. Saleh, B.E.; Teich, M.C.; Saleh, B.E. *Fundamentals of photonics*, second ed.; Vol. 22, Wiley New York, 2007.
10. Gershun, A. The Light Field. *Journal of Mathematics and Physics* **1936**, *18*, 51–151. doi:10.1002/sapm193918151.
11. Lam, E.Y. Computational photography with plenoptic camera and light field capture: tutorial. *Journal of the Optical Society of America* **2015**, *32*, 2021–2032. doi:10.1364/josaa.32.002021.
12. Zheng, J.; Micó, V.; Gao, P. Resolution Enhancement in Phase Microscopy: a Review, 2018. doi:10.20944/preprints201803.0273.v1.
13. Hong, J.; Kim, Y.; Choi, H.J.; Hahn, J.; Park, J.H.; Kim, H.; Min, S.W.; Chen, N.; Lee, B. Three-dimensional display technologies of recent interest: principles, status, and issues. *Applied Optics* **2011**, *50*, H87–H115. doi:10.1364/ao.50.000h87.
14. Park, S.; Yeom, J.; Jeong, Y.; Chen, N.; Hong, J.Y.; Lee, B. Recent issues on integral imaging and its applications. *Journal of Information Display* **2014**, *15*, 37–46. doi:10.1080/15980316.2013.867906.
15. Zhao, Y.; Kwon, K.C.; Piao, Y.; Jeon, S.H.; Kim, N. Depth-layer weighted prediction method for a full-color polygon-based holographic system with real objects. *Optics Letters* **2017**, *42*, 2599. doi:10.1364/ol.42.002599.
16. Li, G.; Hong, K.; Yeom, J.; Chen, N.; Park, J.H.; Kim, N.; Lee*, B. Acceleration method for computer generated spherical hologram calculation of real objects using graphics processing unit. *Chinese Optics Letters* **2014**, *12*, 060016. doi:10.3788/COL201412.060016.
17. Mait, J.N.; Euliss, G.W.; Athale, R.A. Computational imaging. *Advances in Optics and Photonics* **2018**, *10*, 409. doi:10.1364/aop.10.000409.
18. Horisaki, R.; Ogura, Y.; Aino, M.; Tanida, J. Single-shot phase imaging with a coded aperture. *Optics Letters* **2014**, *39*, 6466. doi:10.1364/ol.39.006466.
19. Fienup, J.R. Phase retrieval algorithms: a comparison. *Applied Optics* **1982**, *21*, 2758. doi:10.1364/ao.21.002758.
20. Testorf, M.; Hennelly, B.; Ojeda-Castañeda, J. *Phase-space Optics*; McGraw-Hill Professional Publishing, 2009.
21. Teague, M.R. Deterministic phase retrieval: a Green's function solution. *Journal of the Optical Society of America* **1983**, *73*, 1434–1441. doi:10.1364/josa.73.001434.
22. Gabor, D. A New Microscopic Principle. *Nature* **1948**, *161*, 777–778. doi:10.1038/161777a0.
23. Poon, T.C. *Digital Holography and Three-Dimensional Display: Principles and Applications*; Springer, 2006.
24. Boesl, U. Time-of-flight mass spectrometry: Introduction to the basics. *Mass Spectrometry Reviews* **2016**, *36*, 86–109. doi:10.1002/mas.21520.
25. Geng, J. Structured-light 3D surface imaging: a tutorial. *Advances in Optics and Photonics* **2011**, *3*, 128–160. doi:10.1364/aop.3.000128.
26. Banks, M.S.; Read, J.C.A.; Allison, R.S.; Watt, S.J. Stereoscopic and the Human Visual System. *SMPTE Motion Imaging Journal* **2012**, *121*, 24–43. doi:10.5594/j18173.
27. Orth, A.; Crozier, K.B. Light field moment imaging. *Optics Letters* **2013**, *38*, 2666–2668. doi:10.1364/ol.38.002666.
28. Levoy, M. Light fields and computational imaging. *Computer* **2006**, *39*, 46–55. doi:10.1109/mc.2006.270.
29. Levoy, M.; Ng, R.; Adams, A.; Footer, M.; Horowitz, M. Light field microscopy. *ACM Transactions on Graphics* **2006**, *25*, 924–934. doi:10.1145/1179352.1141976.
30. Ng, R. Fourier slice photography. *ACM Transactions on Graphics* **2005**, *24*, 735–744. doi:10.1145/1186822.1073256.
31. Levoy, M.; Hanrahan, P. Light field rendering. Proceedings of the 23rd Annual Conference on Computer Graphics and Interactive Techniques. ACM, 1996, SIGGRAPH '96, pp. 31–42. doi:10.1145/237170.237199.

32. Xiao, X.; Javidi, B.; Martinez-Corral, M.; Stern, A. Advances in three-dimensional integral imaging: sensing, display, and applications. *Applied Optics* **2013**, *52*, 546–560. doi:10.1364/ao.52.000546.
33. Wilburn, B.; Joshi, N.; Vaish, V.; Talvala, E.V.; Antunez, E.; Barth, A.; Adams, A.; Horowitz, M.; Levoy, M. High performance imaging using large camera arrays. *ACM Transactions on Graphics* **2005**, *24*, 765–776. doi:10.1145/1186822.1073259.
34. Lin, X.; Wu, J.; Zheng, G.; Dai, Q. Camera array based light field microscopy. *Biomedical Optics Express* **2015**, *6*, 3179–3189. doi:10.1364/boe.6.003179.
35. Georgiev, T.; Zheng, K.C.; Curless, B.; Salesin, D.; Nayar, S.; ; Intwala, C. Spatio-angular resolution tradeoffs in integral photography. *Symposium on Rendering* **2006**, *2006*, 21. doi:10.2312/egwr/egsr06/263-272.
36. Veeraraghavan, A.; Raskar, R.; Agrawal, A.; Mohan, A.; Tumblin, J. Dappled Photography: Mask Enhanced Cameras for Heterodyned Light Fields and Coded Aperture Refocusing. *ACM Transactions on Graphics* **2007**, *26*, 69. doi:10.1145/1276377.1276463.
37. Liang, C.K.; Lin, T.H.; Wong, B.Y.; Liu, C.; Chen, H.H. Programmable aperture photography. *ACM Transactions on Graphics* **2008**, *27*, 1. doi:10.1145/1360612.1360654.
38. Fuchs, M.; Kachele, M.; Rusinkiewicz, S. Design and Fabrication of Faceted Mirror Arrays for Light Field Capture. *Computer Graphics Forum*. Wiley Online Library, Wiley, 2013, Vol. 32, pp. 246–257. doi:10.1111/cgf.12201.
39. Manakov, A.; Restrepo, J.F.; Klehm, O.; Hegedüs, R.; Eisemann, E.; Seidel, H.P.; Ihrke, I. A reconfigurable camera add-on for high dynamic range, multispectral, polarization, and light-field imaging. *ACM Transactions on Graphics* **2013**, *32*, 47–1. doi:10.1145/2461912.2461937.
40. Levoy, M.; Zhang, Z.; McDowall, I. Recording and controlling the 4D light field in a microscope using microlens arrays. *Journal of Microscopy* **2009**, *235*, 144–162. doi:10.1111/j.1365-2818.2009.03195.x.
41. Ng, R. Digital light field photography. PhD thesis, Stanford University, Stanford, CA, USA, 2006. doi:10.1117/12.692290.
42. Park, J.H.; Hong, K.; Lee, B. Recent progress in three-dimensional information processing based on integral imaging. *Applied Optics* **2009**, *48*, H77. doi:10.1364/ao.48.000h77.
43. Chen, N.; Park, J.H.; Kim, N. Parameter analysis of integral Fourier hologram and its resolution enhancement. *Optics Express* **2010**, *18*, 2152–2167. doi:10.1364/oe.18.002152.
44. Chen, N.; Yeom, J.; Jung, J.H.; Park, J.H.; Lee, B. Resolution comparison between integral-imaging-based hologram synthesis methods using rectangular and hexagonal lens arrays. *Optics Express* **2011**, *19*, 26917–26927. doi:10.1364/oe.19.026917.
45. Denisyuk, Y.N. On the reflection of optical properties of an object in a wave field of light scattered by it. *Doklady Akademii Nauk SSSR* **1962**, *144*, 1275–1278. doi:10.1117/12.474951.
46. Leith, E.N.; Upatnieks, J. Wavefront Reconstruction with Continuous-Tone Objects. *Journal of the Optical Society of America* **1963**, *53*, 1377. doi:10.1364/josa.53.001377.
47. Ren, Z.; Xu, Z.; Lam, E.Y. Learning-based Nonparametric Autofocusing for Digital Holography. *Optica* **2018**, *5*, 337–344. doi:10.1364/optica.5.000337.
48. Hariharan, P.; Oreb, B.F.; Eiju, T. Digital phase-shifting interferometry: a simple error-compensating phase calculation algorithm. *Applied Optics* **1987**, *26*, 2504–2506. doi:10.1364/ao.26.002504.
49. Chan, A.C.; Tsia, K.K.; Lam, E.Y. Subsampled scanning holographic imaging (SuSHI) for fast, non-adaptive recording of three-dimensional objects. *Optica* **2016**, *3*, 911–917. doi:10.1364/optica.3.000911.
50. Nugent, K.A. X-ray non-interferometric phase imaging: a unified picture. *Journal of the Optical Society of America A* **2007**, *24*, 536. doi:10.1364/josaa.24.000536.
51. Chen, N.; Ren, Z.; Li, D.; Lam, E.Y.; Situ, G. Analysis of the noise in back-projection light field acquisition and its optimization. *Applied Optics* **2017**, *56*, F20–F26. doi:10.1364/ao.56.000f20.
52. Goodman, J.W. *Introduction to Fourier Optics*, third ed.; Roberts & Company, 2005. doi:10.1364/fio.2015.fw3g.1.
53. Park, J.H.; Seo, S.W.; Chen, N.; Kim, N. Fourier hologram generation from multiple incoherent defocused images. *Proc. SPIE*. SPIE, 2010, Vol. 7690, pp. 76900F–76900F–8. doi:10.1117/12.852487.
54. Park, J.H.; Seo, S.W.; Chen, N.; Kim, N. Hologram Synthesis from Defocused Images Captured under Incoherent Illumination. *Biomedical Optics and 3-D Imaging*. OSA, 2010, p. JMA29. doi:10.1364/biomed.2010.jma29.

55. Levin, A.; Durand, F. Linear view synthesis using a dimensionality gap light field prior. *IEEE International Conference on Computer Vision and Pattern Recognition*. IEEE, IEEE, 2010, pp. 1831–1838. doi:10.1109/cvpr.2010.5539854.
56. Xu, Z.; Ke, J.; Lam, E.Y. High-resolution lightfield photography using two masks. *Optics Express* **2012**, *20*, 10971–10983. doi:10.1364/oe.20.010971.
57. Marwah, K.; Wetzstein, G.; Bando, Y.; Raskar, R. Compressive Light Field Photography Using Overcomplete Dictionaries and Optimized Projections. *ACM Transactions on Graphics* **2013**, *32*, 46:1–46:12. doi:10.1145/2461912.2461914.
58. Bailey, S.W.; Echevarria, J.I.; Bodenheimer, B.; Gutierrez, D. Fast depth from defocus from focal stacks. *The Visual Computer* **2014**, *31*, 1697–1708. doi:10.1007/s00371-014-1050-2.
59. Kuthirummal, S.; Nagahara, H.; Zhou, C.; Nayar, S.K. Flexible depth of field photography. *IEEE Transactions on Pattern Analysis and Machine Intelligence* **2011**, *33*, 58–71. doi:10.1109/tpami.2010.66.
60. Zeng, G.L. One-angle fluorescence tomography with in-and-out motion. *Journal of Electronic imaging* **2013**, *22*, 043018. doi:10.1117/1.jei.22.4.043018.
61. McMillan, L.; Bishop, G. Plenoptic modeling: an image-based rendering system. *Proceedings of the 22nd annual conference on Computer graphics and interactive techniques*. ACM, ACM Press, 1995, pp. 39–46. doi:10.1145/218380.218398.
62. Park, J.H.; Lee, S.K.; Jo, N.Y.; Kim, H.J.; Kim, Y.S.; Lim, H.G. Light ray field capture using focal plane sweeping and its optical reconstruction using 3D displays. *Optics Express* **2014**, *22*, 25444–25454. doi:10.1364/oe.22.025444.
63. Mousnier, A.; Vural, E.; Guillemot, C. Partial light field tomographic reconstruction from a fixed-camera focal stack, 2015, [arXiv:1503.01903].
64. Wang, H.; Chen, N.; Zheng, S.; Liu, J.; Situ, G. Fast and high-resolution light field acquisition using defocus modulation. *Applied Optics* **2018**, *57*, A250–A256. doi:10.1364/ao.57.00a250.
65. Wang, H.; Chen, N.; Liu, J.; Situ, G. Light field imaging based on defocused photographic images. *Digital Holography & 3-D Imaging Meeting*; Optical Society of America: Jeju, Korea, 2017. doi:10.1364/DH.2017.W3A.3.
66. Chen, N.; Ren, Z.; Lam, E.Y. High-resolution Fourier hologram synthesis from photographic images through computing the light field. *Applied Optics* **2016**, *55*, 1751. doi:10.1364/ao.55.001751.
67. Liu, J.; Xu, T.; Yue, W.; Sun, J.; Situ, G. Light-field moment microscopy with noise reduction. *Optics Express* **2015**, *23*, 29154–29162. doi:10.1364/oe.23.029154.
68. Zhang, Z.; Levoy, M. Wigner distributions and how they relate to the light field. *IEEE International Conference on Computational Photography (ICCP)*. IEEE, IEEE, 2009, pp. 1–10. doi:10.1109/iccp.2009.5559007.
69. Sun, X.; Meng, N.; Xu, Z.; Lam, E.Y.; So, H.K.H. Sparse Hierarchical Nonparametric Bayesian learning for light field representation and denoising. *IEEE International Joint Conference on Neural Networks*. IEEE, 2016, pp. 3272–3279. doi:10.1109/ijcnn.2016.7727617.
70. Sun, X.; Xu, Z.; Meng, N.; Lam, E.Y.; So, H.K.H. Data-driven light field depth estimation using deep Convolutional Neural Networks. *IEEE International Joint Conference on Neural Networks*. IEEE, 2016, pp. 367–374. doi:10.1109/ijcnn.2016.7727222.
71. Liu, C.; Qiu, J.; Jiang, M. Light field reconstruction from projection modeling of focal stack. *Optics Express* **2017**, *25*, 11377–11388. doi:10.1364/oe.25.011377.
72. Yin, X.; Wang, G.; Li, W.; Liao, Q. Iteratively reconstructing 4D light fields from focal stacks. *Applied Optics* **2016**, *55*, 8457. doi:10.1364/ao.55.008457.
73. Jiang, Z.; Pan, X.; Liu, C.; Wang, L.; Zhu, J. Light field moment imaging with the ptychographic iterative engine. *AIP Advances* **2014**, *4*, 107108. doi:10.1063/1.4897380.
74. Teague, M.R. Irradiance moments: their propagation and use for unique retrieval of phase. *Journal of the Optical Society of America* **1982**, *72*, 1199–1209. doi:10.1364/josa.72.001199.
75. Falaggis, K.; Kozacki, T.; Kujawińska, M.; Józwick, M.; Kuś, A. Optimum plane selection criteria for single-beam phase retrieval techniques based on the contrast transfer function. *Optics Letters* **2014**, *39*, 30–33. doi:10.1007/978-3-642-36359-7_16.

76. Martinez-Carranza, J.; Falaggis, K.; Kozacki, T. Optimum measurement criteria for the axial derivative intensity used in transport of intensity-equation-based solvers. *Optics Letters* **2014**, *39*, 182–185. doi:10.1364/ol.39.000182.
77. Liu, C.; Qiu, J.; Zhao, S. Iterative reconstruction of scene depth with fidelity based on light field data. *Applied Optics* **2017**, *56*, 3185. doi:10.1364/ao.56.003185.
78. Zuo, C.; Chen, Q.; Qu, W.; Asundi, A. High-speed transport-of-intensity phase microscopy with an electrically tunable lens. *Optics Express* **2013**, *21*, 24060–24075. doi:10.1364/oe.21.024060.
79. Gerchberg, R.W.; Saxton, W.O. A practical algorithm for the determination of the phase from image and diffraction plane pictures. *Journal of Physics D: Applied Physics* **1972**, *35*, 237–246. doi:10.1088/0022-3727/6/5/101.
80. Gureyev, T.E.; Roberts, A.; Nugent, K.A. Partially coherent fields, the transport-of-intensity equation, and phase uniqueness. *Journal of the Optical Society of America A* **1995**, *12*, 1942–1946. doi:10.1364/josaa.12.001942.
81. Paganin, D.; Nugent, K.A. Noninterferometric Phase Imaging with Partially Coherent Light. *Physical Review Letters* **1998**, *80*, 2586–2589. doi:10.1103/physrevlett.80.2586.
82. zhen Yang, G.; zhen Dong, B.; yuan Gu, B.; yao Zhuang, J.; Ersoy, O.K. Gerchberg–Saxton and Yang–Gu algorithms for phase retrieval in a nonunitary transform system: a comparison. *Applied Optics* **1994**, *33*, 209. doi:10.1364/ao.33.000209.
83. Fienup, J.R. Reconstruction of an object from the modulus of its Fourier transform. *Optics Letters* **1978**, *3*, 27–29. doi:10.1364/ol.3.000027.
84. Cederquist, J.N.; Fienup, J.R.; Wackerman, C.C.; Robinson, S.R.; Kryskowski, D. Wave-front phase estimation from Fourier intensity measurements. *Journal of the Optical Society of America A* **1989**, *6*, 1020–1026. doi:10.1364/josaa.6.001020.
85. Devaney, A.J.; Chidlaw, R. On the uniqueness question in the problem of phase retrieval from intensity measurements. *Journal of the Optical Society of America* **1978**, *68*, 1352–1354. doi:10.1364/josa.68.001352.
86. Fienup, J.R. Reconstruction of a complex-valued object from the modulus of its Fourier transform using a support constraint. *Journal of the Optical Society of America A* **1987**, *4*, 118–123. doi:10.1364/josaa.4.000118.
87. Rolleston, R.; George, N. Image reconstruction from partial Fresnel zone information. *Applied Optics* **1986**, *25*, 178. doi:10.1364/ao.25.000178.
88. Misell, D.L. An examination of an iterative method for the solution of the phase problem in optics and electron optics: I. Test calculations. *Journal of Physics D: Applied Physics* **1973**, *6*, 2200–2216. doi:10.1088/0022-3727/6/18/305.
89. Fienup, J.R. Lensless coherent imaging by phase retrieval with an illumination pattern constraint. *Optics Express* **2006**, *14*, 498. doi:10.1364/ope.14.000498.
90. Rolleston, R.; George, N. Stationary phase approximations in Fresnel-zone magnitude-only reconstructions. *Journal of the Optical Society of America A* **1987**, *4*, 148–153. doi:10.1364/josaa.4.000148.
91. Dean, B.H.; Bowers, C.W. Diversity selection for phase-diverse phase retrieval. *Journal of the Optical Society of America A* **2003**, *20*, 1490–1504. doi:10.1364/josaa.20.001490.
92. Mayo, S.C.; Miller, P.R.; Wilkins, S.W.; Davis, T.J.; Gao, D.; Gureyev, T.E.; Paganin, D.; Parry, D.J.; Pogany, A.; Stevenson, A.W. Quantitative X-ray projection microscopy: phase-contrast and multi-spectral imaging. *Journal of Microscopy* **2002**, *207*, 79–96. doi:10.1046/j.1365-2818.2002.01046.x.
93. Anand, A.; Pedrini, G.; Osten, W.; Almoró, P. Wavefront sensing with random amplitude mask and phase retrieval. *Optics Letters* **2007**, *32*, 1584–1586. doi:10.1364/ol.32.001584.
94. Almoró, P.F.; Hanson, S.G. Random phase plate for wavefront sensing via phase retrieval and a volume speckle field. *Applied Optics* **2008**, *47*, 2979. doi:10.1364/ao.47.002979.
95. Zhang, F.; Chen, B.; Morrison, G.R.; Vila-Comamala, J.; Guizar-Sicairos, M.; Robinson, I.K. Phase retrieval by coherent modulation imaging. *Nature Communications* **2016**, *7*, 13367. doi:10.1038/ncomms13367.
96. Brady, G.R.; Guizar-Sicairos, M.; Fienup, J.R. Optical wavefront measurement using phase retrieval with transverse translation diversity. *Optics Express* **2009**, *17*, 624. doi:10.1364/oe.17.000624.
97. Rodenburg, J.M.; Faulkner, H.M.L. A phase retrieval algorithm for shifting illumination. *Applied Physics Letters* **2004**, *85*, 4795–4797. doi:10.1063/1.1823034.
98. Pedrini, G.; Osten, W.; Zhang, Y. Wave-front reconstruction from a sequence of interferograms recorded at different planes. *Optics Letters* **2005**, *30*, 833. doi:10.1364/ol.30.000833.

99. Chen, N.; Yeom, J.; Hong, K.; Li, G.; Lee, B. Fast Converging Algorithm for Wavefront Reconstruction based on a Sequence of Diffracted Intensity Images. *Journal of the Optical Society of Korea* **2014**, *18*, 217–224. doi:10.3807/josk.2014.18.3.217.
100. Bao, P.; Zhang, F.; Pedrini, G.; Osten, W. Phase retrieval using multiple illumination wavelengths. *Optics Letters* **2008**, *33*, 309. doi:10.1364/ol.33.000309.
101. Lee, B.; young Hong, J.; Yoo, D.; Cho, J.; Jeong, Y.; Moon, S.; Lee, B. Single-shot phase retrieval via Fourier ptychographic microscopy. *Optica* **2018**, *5*, 976–983. doi:10.1364/optica.5.000976.
102. Zheng, G.; Horstmeyer, R.; Yang, C. Wide-field, high-resolution Fourier ptychographic microscopy. *Nature Photonics* **2013**, *7*, 739–745. doi:10.1038/nphoton.2013.187.
103. Zhou, A.; Chen, N.; Wang, H.; Situ, G. Analysis of Fourier ptychographic microscopy with half of the captured images. *Journal of Optics* **2018**, *20*, 095701. doi:10.1088/2040-8986/aad453.
104. Zhou, A.; Wang, W.; Chen, N.; Lam, E.Y.; Lee, B.; Situ, G. Fast and robust misalignment correction of Fourier ptychographic microscopy for full field of view reconstruction. *Optics Express* **2018**, *26*, 23661–23674. doi:10.1364/oe.26.023661.
105. Gao, P.; Pedrini, G.; Osten, W. Phase retrieval with resolution enhancement by using structured illumination. *Optics Letters* **2013**, *38*, 5204. doi:10.1364/ol.38.005204.
106. Gao, P.; Pedrini, G.; Zuo, C.; Osten, W. Phase retrieval using spatially modulated illumination. *Optics Letters* **2014**, *39*, 3615. doi:10.1364/ol.39.003615.
107. Almoró, P.; Pedrini, G.; Osten, W. Complete wavefront reconstruction using sequential intensity measurements of a volume speckle field. *Applied Optics* **2006**, *45*, 8596. doi:10.1364/ao.45.008596.
108. Camacho, L.; Micó, V.; Zalevsky, Z.; García, J. Quantitative phase microscopy using defocussing by means of a spatial light modulator. *Optics Express* **2010**, *18*, 6755. doi:10.1364/oe.18.006755.
109. Agour, M.; Almoró, P.F.; Falldorf, C. Investigation of smooth wave fronts using SLM-based phase retrieval and a phase diffuser. *Journal of the European Optical Society: Rapid Publications* **2012**, *7*. doi:10.2971/jeos.2012.12046.
110. Almoró, P.F.; Glückstad, J.; Hanson, S.G. Single-plane multiple speckle pattern phase retrieval using a deformable mirror. *Optics Express* **2010**, *18*, 19304. doi:10.1364/oe.18.019304.
111. Roddier, F.; Roddier, C.; Roddier, N. Curvature sensing: a new wavefront sensing method. *Statistical Optics*; Morris, G.M., Ed. International Society for Optics and Photonics, SPIE, 1988, Vol. 976, pp. 203–210. doi:10.1117/12.948547.
112. Bajt, S.; Barty, A.; Nugent, K.; McCartney, M.; Wall, M.; Paganin, D. Quantitative phase-sensitive imaging in a transmission electron microscope. *Ultramicroscopy* **2000**, *83*, 67–73. doi:10.1016/s0304-3991(99)00174-6.
113. Nugent, K.A. Coherent methods in the X-ray sciences. *Advances in Physics* **2010**, *59*, 1–99, [arXiv:physics.optics/0908.3064]. doi:10.1080/00018730903270926.
114. Allman, B.; McMahon, P.; Nugent, K.; Paganin, D.; Jacobson, D.; Arif, M.; Werner, S. Phase radiography with neutrons. *Nature* **2000**, *408*, 158–159. doi:10.1038/35041626.
115. Streibl, N. Phase imaging by the transport equation of intensity. *Optics Communications* **1984**, *49*, 6–10. doi:10.1016/0030-4018(84)90079-8.
116. Barty, A.; Nugent, K.A.; Paganin, D.; Roberts, A. Quantitative optical phase microscopy. *Optics Letters* **1998**, *23*, 817–819. doi:10.1364/ol.23.000817.
117. Kou, S.S.; Waller, L.; Barbastathis, G.; Marquet, P.; Depeursinge, C.; Sheppard, C.J.R. Quantitative phase restoration by direct inversion using the optical transfer function. *Optics Letters* **2011**, *36*, 2671–2673. doi:10.1364/OL.36.002671.
118. Zuo, C.; Chen, Q.; Qu, W.; Asundi, A. Noninterferometric single-shot quantitative phase microscopy. *Optics Letters* **2013**, *38*, 3538–3541. doi:10.1364/OL.38.003538.
119. Zuo, C.; Chen, Q.; Asundi, A. Light field moment imaging: comment. *Optics Letters* **2014**, *39*, 654–654. doi:10.1364/ol.39.000654.
120. Woods, S.C.; Greenaway, A.H. Wave-front sensing by use of a Green's function solution to the intensity transport equation. *Journal of the Optical Society of America A* **2003**, *20*, 508–512. doi:10.1364/JOSAA.20.000508.
121. Allen, L.; Oxley, M. Phase retrieval from series of images obtained by defocus variation. *Optics Communications* **2001**, *199*, 65–75. doi:10.1016/s0030-4018(01)01556-5.

122. Pinhasi, S.V.; Alimi, R.; Perelmutter, L.; Eliezer, S. Topography retrieval using different solutions of the transport intensity equation. *Journal of the Optical Society of America A* **2010**, *27*, 2285–2292. doi:10.1364/JOSAA.27.002285.
123. Gureyev, T.E.; Roberts, A.; Nugent, K.A. Phase retrieval with the transport-of-intensity equation: matrix solution with use of Zernike polynomials. *Journal of the Optical Society of America A* **1995**, *12*, 1932. doi:10.1364/josaa.12.001932.
124. Gureyev, T.E.; Nugent, K.A. Phase retrieval with the transport-of-intensity equation. II. Orthogonal series solution for nonuniform illumination. *Journal of the Optical Society of America A* **1996**, *13*, 1670–1682. doi:10.1364/JOSAA.13.001670.
125. Gureyev, T.E.; Nugent, K.A. Rapid quantitative phase imaging using the transport of intensity equation. *Optics Communications* **1997**, *133*, 339–346. doi:10.1016/S0030-4018(96)00454-3.
126. Zuo, C.; Chen, Q.; Asundi, A. Boundary-artifact-free phase retrieval with the transport of intensity equation: fast solution with use of discrete cosine transform. *Optics Express* **2014**, *22*, 9220–9244. doi:10.1364/OE.22.009220.
127. Zuo, C.; Chen, Q.; Li, H.; Qu, W.; Asundi, A. Boundary-artifact-free phase retrieval with the transport of intensity equation II: applications to microlens characterization. *Optics Express* **2014**, *22*, 18310–18324. doi:10.1364/OE.22.018310.
128. Huang, L.; Zuo, C.; Idir, M.; Qu, W.; Asundi, A. Phase retrieval with the transport-of-intensity equation in an arbitrarily shaped aperture by iterative discrete cosine transforms. *Optics Letters* **2015**, *40*, 1976. doi:10.1364/OL.40.001976.
129. Volkov, V.V.; Zhu, Y.; De Graef, M. A new symmetrized solution for phase retrieval using the transport of intensity equation. *Micron* **2002**, *33*, 411–416. doi:10.1016/S0968-4328(02)00017-3.
130. Martinez-Carranza, J.; Falaggis, K.; Kozacki, T.; Kujawinska, M. Effect of imposed boundary conditions on the accuracy of transport of intensity equation based solvers. Modeling Aspects in Optical Metrology IV; Bodermann, B.; Frenner, K.; Silver, R.M., Eds. SPIE, 2013, p. 87890N. doi:10.1117/12.2020662.
131. Zuo, C.; Chen, Q.; Huang, L.; Asundi, A. Phase discrepancy analysis and compensation for fast Fourier transform based solution of the transport of intensity equation. *Optics Express* **2014**, *22*, 17172. doi:10.1364/oe.22.017172.
132. Ishizuka, K.; Allman, B. Phase measurement of atomic resolution image using transport of intensity equation. *Journal of Electron Microscopy* **2005**, *54*, 191–197. doi:10.1093/jmicro/dfi024.
133. Soto, M.; Acosta, E. Improved phase imaging from intensity measurements in multiple planes. *Applied Optics* **2007**, *46*, 7978–7981. doi:10.1364/ao.46.007978.
134. Cong, W.; Wang, G. Higher-order phase shift reconstruction approach: Higher-order phase shift reconstruction approach. *Medical Physics* **2010**, *37*, 5238–5242. doi:10.1118/1.3488888.
135. Waller, L.; Tian, L.; Barbastathis, G. Transport of intensity phase-amplitude imaging with higher order intensity derivatives. *Optics Express* **2010**, *18*, 12552–12561. doi:10.1364/oe.18.012552.
136. Bie, R.; Yuan, X.H.; Zhao, M.; Zhang, L. Method for estimating the axial intensity derivative in the TIE with higher order intensity derivatives and noise suppression. *Optics express* **2012**, *20*, 8186–8191. doi:10.1364/oe.20.008186.
137. Zuo, C.; Chen, Q.; Yu, Y.; Asundi, A. Transport-of-intensity phase imaging using Savitzky-Golay differentiation filter-theory and applications. *Optics Express* **2013**, *21*, 5346–5362. doi:10.1364/oe.21.005346.
138. Gureyev, T.; Pogany, A.; Paganin, D.; Wilkins, S. Linear algorithms for phase retrieval in the Fresnel region. *Optics Communications* **2004**, *231*, 53–70. doi:10.1016/j.optcom.2003.12.020.
139. Martinez-Carranza, J.; Falaggis, K.; Kozacki, T. Multi-filter transport of intensity equation solver with equalized noise sensitivity. *Optics Express* **2015**, *23*, 23092–23107. doi:10.1364/OE.23.023092.
140. Sun, J.; Zuo, C.; Chen, Q. Iterative optimum frequency combination method for high efficiency phase imaging of absorptive objects based on phase transfer function. *Optics Express* **2015**, *23*, 28031. doi:10.1364/OE.23.028031.
141. Jenkins, M.H.; Long, J.M.; Gaylord, T.K. Multifilter phase imaging with partially coherent light. *Applied Optics* **2014**, *53*, D29–D39. doi:10.1364/AO.53.000D29.
142. Zhong, J.; Claus, R.A.; Dauwels, J.; Tian, L.; Waller, L. Transport of intensity phase imaging by intensity spectrum fitting of exponentially spaced defocus planes. *Optics Express* **2014**, *22*, 10661–10674. doi:10.1364/oe.22.010661.

143. Frank, J.; Altmeyer, S.; Wernicke, G. Non-interferometric, non-iterative phase retrieval by Green's functions. *Journal of the Optical Society of America A* **2010**, *27*, 2244–2251. doi:10.1364/JOSAA.27.002244.
144. Ishizuka, A.; Mitsuishi, K.; Ishizuka, K. Direct observation of curvature of the wave surface in transmission electron microscope using transport intensity equation. *Ultramicroscopy* **2018**, *194*, 7–14. doi:10.1016/j.ultramic.2018.06.010.
145. Ishizuka, A.; Ishizuka, K.; Mitsuishi, K. Boundary-artifact-free Observation of Magnetic Materials Using the Transport of Intensity Equation. *Microscopy and Microanalysis* **2018**, *24*, 924–925. doi:10.1017/S1431927618005111.
146. Schmalz, J.A.; Gureyev, T.E.; Paganin, D.M.; Pavlov, K.M. Phase retrieval using radiation and matter-wave fields: Validity of Teague's method for solution of the transport-of-intensity equation. *Physical Review A* **2011**, *84*. doi:10.1103/PhysRevA.84.023808.
147. Ferrari, J.A.; Ayubi, G.A.; Flores, J.L.; Perciante, C.D. Transport of intensity equation: Validity limits of the usually accepted solution. *Optics Communications* **2014**, *318*, 133–136. doi:10.1016/j.optcom.2013.12.060.
148. Paganin, D.; Barty, A.; McMahon, P.J.; Nugent, K.A. Quantitative phase-amplitude microscopy. III. The effects of noise. *Journal of microscopy* **2004**, *214*, 51–61. doi:10.1111/j.0022-2720.2004.01295.x.
149. Martin, A.; Chen, F.R.; Hsieh, W.K.; Kai, J.J.; Findlay, S.; Allen, L. Spatial incoherence in phase retrieval based on focus variation. *Ultramicroscopy* **2006**, *106*, 914–924. doi:10.1016/j.ultramic.2006.04.008.
150. Xue, B.; Zheng, S.; Cui, L.; Bai, X.; Zhou, F. Transport of intensity phase imaging from multiple intensities measured in unequally-spaced planes. *Optics Express* **2011**, *19*, 20244–20250. doi:10.1364/OE.19.020244.
151. Zheng, S.; Xue, B.; Xue, W.; Bai, X.; Zhou, F. Transport of intensity phase imaging from multiple noisy intensities measured in unequally-spaced planes. *Optics Express* **2012**, *20*, 972–985. doi:10.1364/OE.20.000972.
152. Savitzky, A.; Golay, M.J.E. Smoothing and Differentiation of Data by Simplified Least Squares Procedures. *Analytical Chemistry* **1964**, *36*, 1627–1639. doi:10.1021/ac60214a047.
153. Gorry, P.A. General least-squares smoothing and differentiation of nonuniformly spaced data by the convolution method. *Analytical chemistry* **1991**, *63*, 534–536. doi:10.1021/ac00005a031.
154. Luo, J.; Ying, K.; He, P.; Bai, J. Properties of Savitzky–Golay digital differentiators. *Digital Signal Processing* **2005**, *15*, 122–136. doi:10.1016/j.dsp.2004.09.008.
155. Zuo, C.; Sun, J.; Zhang, J.; Hu, Y.; Chen, Q. Lensless phase microscopy and diffraction tomography with multi-angle and multi-wavelength illuminations using a LED matrix. *Optics Express* **2015**, *23*, 14314. doi:10.1364/OE.23.014314.
156. Waller, L.; Kou, S.S.; Sheppard, C.J.R.; Barbastathis, G. Phase from chromatic aberrations. *Optics Express* **2010**, *18*, 22817–22825. doi:10.1364/OE.18.022817.
157. Nguyen, T.; Nehmetallah, G.; Tran, D.; Darudi, A.; Soltani, P. Fully automated, high speed, tomographic phase object reconstruction using the transport of intensity equation in transmission and reflection configurations. *Applied Optics* **2015**, *54*, 10443–10453. doi:10.1364/AO.54.010443.
158. Almoró, P.F.; Waller, L.; Agour, M.; Falldorf, C.; Pedrini, G.; Osten, W.; Hanson, S.G. Enhanced deterministic phase retrieval using a partially developed speckle field. *Optics letters* **2012**, *37*, 2088–2090. doi:10.1364/ol.37.002088.
159. Gorthi, S.S.; Schonbrun, E. Phase imaging flow cytometry using a focus-stack collecting microscope. *Optics letters* **2012**, *37*, 707–709. doi:10.1364/ol.37.000707.
160. Zuo, C.; Sun, J.; Li, J.; Zhang, J.; Asundi, A.; Chen, Q. High-resolution transport-of-intensity quantitative phase microscopy with annular illumination. *Scientific Reports* **2017**, *7*, 7654. doi:10.1038/s41598-017-06837-1.
161. Li, J.; Chen, Q.; Zhang, J.; Zhang, Y.; Lu, L.; Zuo, C. Efficient quantitative phase microscopy using programmable annular LED illumination. *Biomedical Optics Express* **2017**, *8*, 4687–4705. doi:10.1364/BOE.8.004687.
162. Chakraborty, T.; Petrucci, J.C. Source diversity for transport of intensity phase imaging. *Optics Express* **2017**, *25*, 9122–9137. doi:10.1364/OE.25.009122.
163. Chakraborty, T.; Petrucci, J.C. Optical convolution for quantitative phase retrieval using the transport of intensity equation. *Applied Optics* **2018**, *57*, A134. doi:10.1364/AO.57.00A134.

164. Zuo, C.; Chen, Q.; Qu, W.; Asundi, A. Direct continuous phase demodulation in digital holography with use of the transport-of-intensity equation. *Optics Communications* **2013**, *309*, 221–226. doi:10.1016/j.optcom.2013.07.013.
165. Zuo, C.; Chen, Q.; Asundi, A. Comparison of Digital Holography and Transport of Intensity for Quantitative Phase Contrast Imaging. In *Fringe 2013*; Osten, W., Ed.; Springer Berlin Heidelberg: Berlin, Heidelberg, 2014; pp. 137–142. doi:10.1007/978-3-642-36359-7_17.
166. Gureyev, T.E.; Paganin, D.M.; Stevenson, A.W.; Mayo, S.C.; Wilkins, S.W. Generalized Eikonal of Partially Coherent Beams and Its Use in Quantitative Imaging. *Physical Review Letters* **2004**, *93*, 068103. doi:10.1103/PhysRevLett.93.068103.
167. Zysk, A.M.; Schoonover, R.W.; Carney, P.S.; Anastasio, M.A. Transport of intensity and spectrum for partially coherent fields. *Optics Letters* **2010**, *35*, 2239–2241. doi:10.1364/OL.35.002239.
168. Petrucci, J.C.; Tian, L.; Barbastathis, G. The transport of intensity equation for optical path length recovery using partially coherent illumination. *Optics Express* **2013**, *21*, 14430–14441. doi:10.1364/OE.21.014430.
169. Zuo, C.; Chen, Q.; Tian, L.; Waller, L.; Asundi, A. Transport of intensity phase retrieval and computational imaging for partially coherent fields: The phase space perspective. *Optics and Lasers in Engineering* **2015**, *71*, 20–32. doi:10.1016/j.optlaseng.2015.03.006.
170. Langer, M.; Cloetens, P.; Guigay, J.P.; Peyrin, F. Quantitative comparison of direct phase retrieval algorithms in in-line phase tomography. *Medical Physics* **2008**, *35*, 4556–4566. doi:10.1118/1.2975224.
171. Gureyev, T.E. Composite techniques for phase retrieval in the Fresnel region. *Optics Communications* **2003**, *220*, 49–58. doi:10.1016/S0030-4018(03)01353-1.
172. Guigay, J.P.; Langer, M.; Boistel, R.; Cloetens, P. Mixed transfer function and transport of intensity approach for phase retrieval in the Fresnel region. *Optics Letters* **2007**, *32*, 1617–1619. doi:10.1364/ol.32.001617.
173. Greenbaum, A.; Zhang, Y.; Feizi, A.; Chung, P.L.; Luo, W.; Kandukuri, S.R.; Ozcan, A. Wide-field computational imaging of pathology slides using lens-free on-chip microscopy. *Science Translational Medicine* **2014**, *6*, 267ra175–267ra175. doi:10.1126/scitranslmed.3009850.
174. Zhang, J.; Chen, Q.; Li, J.; Sun, J.; Zuo, C. Lensfree dynamic super-resolved phase imaging based on active micro-scanning. *Optics Letters* **2018**, *43*, 3714. doi:10.1364/ol.43.003714.
175. Shaked, N.T.; Katz, B.; Rosen, J. Review of three-dimensional holographic imaging by multiple-viewpoint-projection based methods. *Applied Optics* **2009**, *48*, H120. doi:10.1364/ao.48.00h120.
176. McCrickerd, J.T.; George, N. Holographic stereogram from sequential component photographs. *Applied Physics Letters* **1968**, *12*, 10–12. doi:10.1063/1.1651831.
177. Benton, S.A. Survey of holographic stereograms. *Processing and Display of Three-Dimensional Data*; Pearson, J.J., Ed. SPIE, 1983. doi:10.1117/12.934296.
178. Tian, L.; Waller, L. 3D intensity and phase imaging from light field measurements in an LED array microscope. *Optica* **2015**, *2*, 104. doi:10.1364/optica.2.000104.
179. Park, J.H.; Baasantseren, G.; Kim, N.; Park, G.; Kang, J.M.; Lee, B. View image generation in perspective and orthographic projection geometry based on integral imaging. *Optics Express* **2008**, *16*, 8800. doi:10.1364/oe.16.008800.
180. Ko, J.; Davis, C.C. Comparison of the plenoptic sensor and the Shack–Hartmann sensor. *Applied Optics* **2017**, *56*, 3689. doi:10.1364/ao.56.003689.
181. Adelson, E.H.; Bergen, J.R. The plenoptic function and the elements of early vision. *Computational models of visual processing* **1991**, *1*. doi:10.1.1.2.9848.
182. Bastiaans, M.J. Application of the Wigner distribution function to partially coherent light. *Journal of the Optical Society of America A, Optics and Image Science* **1986**, *3*, 1227–1238. doi:10.1364/JOSAA.3.001227.
183. Walther, A. Radiometry and Coherence. *Journal of the Optical Society of America* **1968**, *58*, 1256–1259. doi:10.1364/JOSA.58.001256.
184. Boashash, B. Estimating and interpreting the instantaneous frequency of a signal. I. Fundamentals. *Proceedings of the IEEE* **1992**, *80*, 520–538. doi:10.1109/5.135376.
185. Bastiaans, M. The Wigner distribution function applied to optical signals and systems. *Optics Communications* **1978**, *25*, 26–30. doi:10.1016/0030-4018(78)90080-9.
186. Winston, R.; Welford, W.T. Geometrical vector flux and some new nonimaging concentrators. *Journal of the Optical Society of America* **1979**, *69*, 532–536. doi:10.1364/JOSA.69.000532.

187. Dragoman, D. Phase-space interferences as the source of negative values of the Wigner distribution function. *Journal of the Optical Society of America A, Optics and Image Science* **2000**, *17*, 2481–2485. doi:10.1364/JOSAA.17.002481.
188. Bastiaans, M.J. Uncertainty principle for partially coherent light. *Journal of the Optical Society of America* **1983**, *73*, 251–255. doi:10.1364/JOSA.73.000251.
189. Paganin, D.; Gureyev, T.E.; Mayo, S.C.; Stevenson, A.W.; Nesterets, Y.I.; Wilkins, S.W. X-ray omni microscopy. *Journal of Microscopy* **2004**, *214*, 315–327. doi:10.1111/j.0022-2720.2004.01315.x.
190. Li, J.; Chen, Q.; Sun, J.; Zhang, J.; Zuo, C. Multimodal computational microscopy based on transport of intensity equation. *Journal of Biomedical Optics* **2016**, *21*, 126003. doi:10.1117/1.JBO.21.12.126003.
191. Friberg, A.T. On the existence of a radiance function for finite planar sources of arbitrary states of coherence. *Journal of the Optical Society of America* **1979**, *69*, 192–198. doi:10.1364/JOSA.69.000192.
192. Oh, S.B.; Kashyap, S.; Garg, R.; Chandran, S.; Raskar, R. Rendering Wave Effects with Augmented Light Field. *Computer Graphics Forum* **2010**, *29*, 507–516. doi:10.1111/j.1467-8659.2009.01620.x.
193. Schwiegerling, J. Wavefront Sensing: Shack-Hartmann Sensing. *Journal of Refractive Surgery* **2001**, *17*, 573–7. doi:10.1117/3.592975.p47.
194. Waller, L. Phase imaging with partially coherent light. Three-Dimensional and Multidimensional Microscopy: Image Acquisition and Processing XX; Cogswell, C.J.; Brown, T.G.; Conchello, J.A.; Wilson, T., Eds. SPIE, 2013, Vol. 8589, pp. 85890K–85890K–6. doi:10.1117/12.2020806.
195. Iaconis, C.; Walmsley, I.A. Direct measurement of the two-point field correlation function. *Optics Letters* **1996**, *21*, 1783–1785. doi:10.1364/OL.21.001783.
196. Marks, D.L.; Stack, R.A.; Brady, D.J. Three-dimensional coherence imaging in the Fresnel domain. *Applied Optics* **1999**, *38*, 1332–1342. doi:10.1364/AO.38.001332.
197. Nugent, K.A. Wave field determination using three-dimensional intensity information. *Physical Review Letters* **1992**, *68*, 2261–2264. doi:10.1103/PhysRevLett.68.2261.
198. Raymer, M.G.; Beck, M.; McAlister, D. Complex wave-field reconstruction using phase-space tomography. *Physical Review Letters* **1994**, *72*, 1137–1140. doi:10.1103/PhysRevLett.72.1137.
199. Rydberg, C.; Bengtsson, J. Numerical algorithm for the retrieval of spatial coherence properties of partially coherent beams from transverse intensity measurements. *Optics Express* **2007**, *15*, 13613. doi:10.1364/OE.15.013613.
200. Zhang, Z.; Chen, Z.; Rehman, S.; Barbastathis, G. Factored form descent: a practical algorithm for coherence retrieval. *Optics Express* **2013**, *21*, 5759. doi:10.1364/OE.21.005759.
201. Tian, L.; Zhang, Z.; Petrucci, J.C.; Barbastathis, G. Wigner function measurement using a lenslet array. *Optics Express* **2013**, *21*, 10511. doi:10.1364/oe.21.010511.
202. Waller, L.; Situ, G.; Fleischer, J.W. Phase-space measurement and coherence synthesis of optical beams. *Nature Photonics* **2012**, *6*, 474–479. doi:10.1038/nphoton.2012.144.
203. Ng, R.; Levoy, M.; Brédif, M.; Duval, G.; Horowitz, M.; Hanrahan, P. Light field photography with a hand-held plenoptic camera. Technical Report 11, 2005. doi:10.1117/12.692290.
204. Park, J.H.; Kim, M.S.; Baasantseren, G.; Kim, N. Fresnel and Fourier hologram generation using orthographic projection images. *Optics Express* **2009**, *17*, 6320–6334. doi:10.1364/oe.17.006320.
205. Shaked, N.T.; Rosen, J.; Stern, A. Integral holography: white-light single-shot hologram acquisition. *Optics Express* **2007**, *15*, 5754–5760. doi:10.1364/oe.15.005754.